

The May 2024 Event in the Context of Auroral Activity over the past 375 years

Mike Lockwood,^{1,5*} Mathew J. Owens,^{1,6} William Brown,² and Manuel Vázquez^{3,4}

¹University of Reading, Department of Meteorology, Whiteknights Campus, Earley Gate, Reading, Berkshire, RG6 6ET, UK

²British Geological Survey, The Lyell Centre, Edinburgh EH14 4AS, UK

³Instituto de Astrofísica de Canarias, 38205 La Laguna, Spain

⁴Departamento de Astrofísica, Universidad de La Laguna, 38205, La Laguna, Spain

⁵(Orcid ID: 0000-0002-7397-2172)

⁶(Orcid ID: 0000-0003-2061-2453)

Accepted XXX. Received YYY; in original form ZZZ

ABSTRACT

We survey auroral records from the Northern Hemisphere for the interval January 1650–July 2024, making full allowance for the secular change in the geomagnetic field. We generate criteria for defining extreme auroral events that are met on 0.015% of nights since 1650 and on 0.023% of nights since 1790. After discussing biases and trends in the data, we compare the recent event of 10–11 May 2024 with other extreme auroral storms and investigate the connection to geomagnetic and sunspot activity of these extreme events. Ranking the events by the lowest geomagnetic latitude from which aurora was observed on a given night, the second night of the May 2024 event is shown to be the 3rd most extensive event known, the most extensive being the “Secchi Event” of 4 February 1872. We find that the area of the sunspot group from where the causal Coronal Mass Ejection arises (identified by the associated white-light flare in historic events and from EUV flare and coronagraph images for modern ones) is not a predictor of the auroral and geomagnetic response: indeed that area is found to be weakly anti-correlated with the terrestrial responses surveyed. However, the scatter is large so that, although the Secchi event arose from a rather small sunspot group, the May 2024 event arose from a large group, as did the “Carrington Events” of August/September 1859 (ranked 2, 4 and 5 by auroral extent, the first night of the May 2024 event being ranked 6). We show that the extreme aurora events all occur during Carrington Rotations for which the average open solar flux, F_S is high (exceeding 4×10^{14} Wb) but only 3.6% of Carrington Rotations when F_S exceeds this value give an extreme event at Earth.

Key words: planets and satellites: aurorae – solar–terrestrial relations – planets and satellites: magnetic fields

1 INTRODUCTION

Aurora is caused by charged particles precipitating into the upper atmosphere. These may have originated in the solar wind by flowing along open field lines into the magnetosphere (Onsager & Lockwood 1997), but many will have moved up field lines from the ionosphere, where they were generated by the photo-ionizing extreme ultraviolet (EUV) and X-ray radiations by the Sun (Welling et al. 2015). The balance between these plasma sources varies with the solar–terrestrial activity level. From the charge-state of ions in the inner plasma sheet of the magnetosphere, the source region of auroral electrons before they are accelerated towards Earth (Kletzing et al. 2003; Sergeev et al. 2020), we know that in quiet times the solar source dominates but in disturbed times (i.e., *storms*) it is the ionospheric source that dominates (Kistler 2020). These charged particles are energized in the magnetosphere by the release of energy that had been extracted from the solar wind and stored in the geomagnetic field. The auroral particles precipitate down field lines and stimulate the emission of auroral light by atoms and molecules in the upper atmosphere.

The bands of latitudes around the geomagnetic poles where aurora most frequently occurs are called the *auroral ovals*. This term has meaning at an instant of time, as well as statistically, because the aurora usually forms complete and continuous rings around the magnetic poles. During periods of high solar wind activity, when the power extracted from the solar wind is very high, the aurora grows in intensity and the ovals expand in both width and radius, bringing aurora to lower latitudes. These events are accompanied by large disturbances to Earth’s magnetic field and are called *geomagnetic storms*.

The nights of 10 and 11 May 2024 are the latest example of a great auroral and geomagnetic storm, in which aurora is seen at exceptionally low latitudes. Such events have been the focus of a great many academic studies over many years (e.g. Silverman 1995, 2006, 2008; Silverman & Cliver 2001; Hayakawa et al. 2018a,b, 2023b,a; Green & Boardsen 2006; González-Esparza & Cuevas-Cardona 2018; Vázquez & Vaquero 2010; Boteler 2019; Allen et al. 1989; Love et al. 2019a; Love & Coisson 2016; McNish 1941; Vichare et al. 2024; Kubota et al. 2017; Livesey 2000, 1984; Valach et al. 2019; Carapiperis 1956; Hapgood 2019; Abbott & Chapman 1959; Berrilli & Giovannelli 2022). Some of these papers focus on

* E-mail: m.lockwood@reading.ac.uk

the societal effects of the storms, others on the morphology and temporal development of the storm, while others analyse the causal solar wind disturbance. The causes and effects of the May 2024 event have recently been reviewed in detail by Hayakawa et al. (2024) and citizen science reports on the event have been used to study the auroral morphology by Grandin et al. (2024). Between 2 May and 9 May 2024, a sunspot group traversing quite close to the centre of the solar disc (designated the identification number 13664 by the NOAA scheme) grew in total whole-spot area (the area of all umbrae and penumbrae in the group) from $113\mu\text{sh}$ to $2761\mu\text{sh}$ (where $1\mu\text{sh}$ is a millionth of a solar hemisphere). Before it had rotated off the solar disc, it had generated 14 “X-class” flares and released 19 large CMEs (Coronal Mass Ejections with longitudinal width exceeding 14°), 10 of which were Earth-directed “halo” events. The combined effect of these CMEs hitting Earth’s magnetosphere generated aurora at low and middle latitudes all round the globe.

Knipp et al. (2021) have put such extremely large space-weather events into context using a “timeline” representation. These authors also make the point that ground-based auroral observations have been a rather imprecise way of studying storms in the past. The reason is the large number of complicating factors that determine if an aurora is recorded, even if it is present at a given location. Perhaps the most obvious vagary is cloud cover: very intense aurora can be detected if cloud cover is thin or broken, but many displays are hidden from view by cloud. Secondly, there is the timing of the peak of the storm. The lowest latitudes of the aurora are around local magnetic midnight (Magnetic Local Time, *MLT*, is around *0hrs*) (Grandin et al. 2024) and so the Universal Time (UTC) of the storm alters the longitude at which the lowest latitudes will occur. This modulates the occurrence of reports, even from cloud-free locations, because of the geographical distribution of potential observers. A key factor in this is the distribution of human populations and reports are more common where population density is high, but with the complication that light pollution by street lighting in cities reduces the potential to see an aurora. However, the presence of humans is not sufficient: a fraction of those humans must be interested enough and able to observe, accurately record and publish their observation.

During storms, some aurora is seen that is similar to that seen in the quiet or moderately disturbed periods, but is more intense and at lower latitudes. Visually, this aurora is either green in colour (the 557.7nm atomic oxygen line arising from a transition from the 1S to the 1D electronic state) or with red above the green (the red being the 630nm atomic oxygen line arising from the transition from the 1D to the ground, 3P , state). These auroras mainly originate from precipitating electrons of energies ranging from 100eV to 100keV (Rees 1969). The red is not seen for the more energetic electrons because they precipitate to lower altitudes in the upper atmosphere (to of order $100\text{-}120\text{km}$) where the long lifetime of the 1D state (110s on average) means that the de-excitation is usually by collision rather than photon emission: the red line is *collisionally quenched* whereas the green line is not because of the shorter (0.8s) average lifetime of the 1S excited state. However, the electrons at the lower end of the energy range only precipitate to greater altitudes (from about 150km to a maximum near 500km) where they have enough energy to excite the 1D state but not the 1S state and at these altitudes the number densities, and hence collision frequency, is sufficiently low that the long-lifetime 1D state can de-excite by emitting a red photon.

However, there is a second class of red aurora that appears during storms at lower latitudes. These last for several hours and usually occur when a sequence of magnetospheric substorms is in progress during a storm (Tinsley et al. 1986; Miyaoka et al. 1990; Rassoul et al. 1992; Shiokawa et al. 1994). These photons are red or blue/purple

in colour. The red is the 630nm line of atomic oxygen discussed above, the blue and purple is from vibrationally excited molecular nitrogen (Tinsley et al. 1984). A notable feature of these auroras is a very high red-to-green intensity emission ratio from atomic oxygen (Mikhalev 2024). Later, during the recovery phase of the storm, monochromatic red-line SAR (Stable Auroral Red) arcs form at these lower latitudes (Kozyra et al. 1997). SAR arcs are thought to be generated by downward heat conduction carried by low-energy ($< 10\text{eV}$) electron precipitation that is produced when high energy ring-current particles interact with the low-energy denser plasma in the plasmasphere: the outer plasmasphere is emptied during the initial phase of the storm as enhanced magnetospheric convection carries a plume of plasmaspheric material to the dayside magnetopause where it is lost to the magnetosheath when the field lines are opened by magnetic reconnection in the magnetopause (Zhang et al. 2018). After they have been re-closed by reconnection in the geomagnetic tail, these flux tubes are then refilled from the top-down by plasma upflow from the ionosphere below as they convect back along the dawn and dusk segments of the auroral oval to the dayside where ionospheric plasma densities are higher): this refilling takes place in quiet periods after the storm (Denton & Borovsky 2014). The red auroras seen during the initial main phase of the storm appear to be caused by a somewhat similar mechanism to SAR arcs, but their onsets are because of a very large storm-time increase in ring current ion fluxes which interact with the depleting plasmasphere in the midnight sector (Shiokawa et al. 2013). This being the case, the migration of these red aurora to very low-latitudes during storms occurs because of the Earthward intrusion of the ring current at midnight (Kataoka et al. 2024), as seen in Energetic Neutral Atom (ENA) imaging of the ring current during storms (Shiokawa et al. 2013).

Comparing modern events, such as the May 2024 storm, with historic observations is difficult. The human population has increased in numbers and spread into some areas of the globe that were previously only sparsely inhabited. In addition, with modern cameras and smartphones, which are generally more sensitive than the human eye, we have provided observers with better means to record the phenomenon. Thirdly, social media, dedicated space weather internet sites and citizen science projects such as *AuroraReach*, *Skywarden* and *Aurorasaurus* give an easier and ready means to disseminate an observation. Lastly, improved forecasting now gives potential observers warning of probable events.

However, these advances have only improved recording of aurora over, approximately, the last 20 years. Before then, records came from the diaries of scientists and enthusiasts, log books generated by observatories, expeditions and commercial ships, meteorological reports and newspaper reports. There are other, unexpected, sources. For example, because a bombing raid on London during the 1914–1918 war had been facilitated by the illumination of the River Thames by aurora (navigation techniques at night were minimal at the time), the British Air Ministry thereafter collected auroral sightings and many were provided by the many lighthouse keepers around the coasts of Britain (Lockwood & Barnard 2015). Logbooks of ships at sea are a small but valuable resource because they help to fill in some of the gaps between centres of population. However, all of these sources of information on the aurora were in decline from about 1950 onwards and before the internet became a factor, auroral reporting was at a lower level than at any time since the 18th century. Reports in newspapers and the literature have become restricted to major events and newspapers often now carry more forecasts of auroral events than after-the-fact reports on them.

These factors mean that it is not straightforward to compare the

May 2024 event to past events. In this paper, we present a method that is designed to try to minimize the effect of the changes and put the 2024 May event in context with other great storms. This is important because in all reconstruction work we aim to make the historic dataset as homogeneous as possible so that we can extrapolate data taken during the space age back to earlier times, as has been done for both continuous data series (e.g., [Lockwood et al. 2022a,b](#)) and for extreme events ([Cliver et al. 2022](#)).

2 METHODS

This paper studies auroral observations in the interval January 1650 to June 2024 to place the major, global auroral event of 10–11 May 2024 in context. Because of the complications mentioned in Section 1 we need to formulate a method to process auroral observation data.

2.1 Processing of auroral samples

This paper combines several catalogues of auroral observations. These include early ones by [Frobesius \(1739\)](#), [Mairan \(1754\)](#), [Boué \(1856\)](#), [Wolf \(1857\)](#), [Lovering \(1868\)](#), and subsequent papers in the series), [Fritz \(1873\)](#), [Seydl \(1954\)](#), [Angot \(1896\)](#) and [Křížský & Pejml K. \(1999\)](#). To these were added the later extensive collections of Sam Silverman that covered the US, Canada and Greenland (now held by the National Space Science Data Centre, NASA Goddard Space Flight Center). Also included are observations found in searches by the authors Manuel Vázquez (Europe) and Mike Lockwood (UK) ([Lockwood & Barnard 2015](#)). In addition, we have added verifiable observations reported in the literature, newspapers and on the internet to bring the collection up to July 2024. A relatively small numbers of records available from academic papers have also been added.

After removing explicit duplicates (i.e., ones where the provenance is recorded and reveals duplication) and inferred duplicates (i.e. with the same named location and/or with the same or very similar coordinates) these surveys together give over 0.2 million auroral reports.

Given that we want the database to as homogeneous as possible, we have to be aware of the effects of changes in human population (number and distribution), their behaviour and the technologies available to them. Modern observations are recorded on the internet via image contributions to space weather sites and social media, and via citizen science activities. That these reports usually give an image of the sighting is useful as one has a chance to identify and discount glows that are light pollution, airglow, sprites, elves, blue-jets, haloes or nacreous clouds. These images are generally recorded on smartphones or using higher-resolution and higher-sensitivity cameras. These can have considerably greater sensitivity than the human eye [Hayakawa et al. \(2024\)](#), so low-intensity aurora can now be recorded that might not have been noted by visual observers in the past. However, the difference between cameras and the eye depends on wavelength, and so auroras of different colours are differently affected. In most cases, the photographer has seen the aurora visually before pointing the camera, so observing may not have been as altered by modern cameras as much as one might imagine. Nevertheless, we note that one image of aurora on May 10 from the Big Island, Hawaii arose because the observer was photographing meteors and only later realized that there was a backdrop of auroral light that his camera had detected where his eyes had not. (However, in this particular case, other accounts from the Big Island that night are specific in saying the observer saw the aurora visually before taking the photograph.)

To help maintain some consistency with historic observations, we do not use any long exposure images nor images taken from aircraft. Unfortunately, fakes are a childish yet growing problem with internet records. At present, an experienced observer can readily identify AI-generated and heavily photo-shopped auroral images; however, that might change in the near future as AI becomes more sophisticated. More difficult to identify are genuine images of past auroral events posted with fake location and/or time labels. Usually the images chosen for this are the most striking ones, and internet image searches provide a way of checking the true provenance. In addition, images of multiple green arcs, characteristic of high latitude aurora, are often attributed to low latitude sites where a diffuse red glow is much more likely. In the current survey, about 500 observations were rejected after such checks. The number of individuals perpetrating these fakes is fortunately small, and their (on-line) names can help identify culprits. For modern data, we do not use observations that are more than 10° equatorward in magnetic latitude than any other observation on that night (or the previous or next night) and this removes many of the observations suspected of being spurious. Area-combined samples (see below) based on only one observation are particularly scrutinized and rejected if their magnetic latitude is below the 2σ point of the overall distribution, unless it is from a trusted source (such as an observatory or a known researcher in the field) and/or corroborated by one or more independent report.

Another great change is the population of humans and their distribution. The important element of the population are the individuals that have the interest to make an observation, often travelling as tourists to auroral latitudes, and the means to record and report them. Hence, population growth, education, auroral tourism, cameras, and the internet, have all acted to increase the number of recorded auroral sightings in the past 3 decades. Unfortunately, this rise came after a fall when newspapers took less interest and specialist laboratories closed or turned their attention to other phenomena.

We use only northern-hemisphere observations in order to maintain a degree of consistency over the past 400 years. Observations from the Southern Hemisphere are rarer because a much larger fraction of that hemisphere at auroral latitudes that is covered by oceans, and recorded observations at sea are much rarer than from on land. However, using data from only one hemisphere has the disadvantage of introducing an annual modulation into the data due to the tilt of the Earth's rotational axis with respect to the ecliptic and the fact that aurora is usually very hard to detect in sunlight. In summer, this makes aurora almost completely undetectable at high geographic latitudes and reduces the hours in a day during which it can be seen from middle latitudes. Were observations as common from the Southern as the Northern Hemisphere, this annual variation could be eliminated by using data from both hemispheres. However, that is not the case, and so we would have an annual modulation of the data even if we included Southern Hemisphere observations. Aurora is ordered by geomagnetic latitude, which varies with geographic latitude and longitude (due to the offset of the geomagnetic and rotational axes) and with date because the secular variation in Earth's magnetic field causes changes to the relative orientation of those two axes.

There are further complications. Earth's magnetic axis is not geocentric and its eccentricity causes Universal Time (UT) variations in solar wind-magnetosphere coupling [Lockwood & Milan \(2023\)](#); [Lockwood \(2023\)](#) and this means that the arrival time of an interplanetary disturbance alters the effect that it has and there are longitudinal differences in the response [Lockwood et al. \(2023\)](#).

Although explicit duplications of observations have been removed, many remain. This is inevitable as catalogues of auroral recordings often contain records of an auroral observation that are carried for-

ward from a prior catalogue (without giving the provenance) and site names or the location coordinates have been updated and/or slightly adjusted. This means that combining catalogues can cause duplicated records that are not always recognized as such. In addition, when surveying historic newspaper reports, the same observation is often reported differently by different newspapers. To avoid undue weight being given to multiple records to what may have been a single observation of aurora, we here use a new approach. Records on a given night that are within 0.2° of each other along the great-circle path (about 22 km in distance) are here treated as just one independent sample that is given the mean latitude and longitude of the combined reports. The angular separation of 0.2° was chosen after a sensitivity study of the balance between the number of observations that are combined and the loss of spatial resolution. This process yields 191660 independent area-combined samples from the total of 216321 reports on 136966 nights. Note that the number of area-combined samples is only approximately 11% smaller than the number of observation reports. A consequence of this is that samples from rural areas often result from a single reported observation, but some samples from major centres of population (without strong street lighting) can result from recordings from several tens of observers. Although multiple observers give greater credence to the observation, without this process the geographical distribution of population (specifically, the population able and willing to record their observation) would even more strongly modulate the statistics of auroral occurrence in a way that changes with time.

Neither the colour nor the position in the sky is considered because it is a relatively small subset of historic observations that give this information. [Grandin et al. \(2024\)](#) have studied citizen science reports from the May 2024 event from the *Aurorasaurus* and *Skywarden* projects and find the distributions in magnetic latitude of reports of predominantly green and predominantly red aurora were very similar at geomagnetic latitudes above 47° but red dominated below this latitude. The nature of the observation site identifier given varies widely. In a very small number of cases it is coordinates (computed with varying degrees of accuracy); in other cases, it is a specific building or monument that can be pinpointed to a few tens of metres; others give the name of a small village or town or a district within a city. However, many just give the name of the town, city or state or even just the country. The distance from an observer who sees a coronal (overhead) auroral form to a second observer who can see the same portion of aurora-lit sky at an elevation of at least 20° above the horizon is, respectively, 230 km, 310 km and 690 km for emission altitudes of 90 km (roughly the base of the oxygen green line emission), 120 km (roughly the top of the green line emission) and 300 km (typical emission height for the oxygen red line). These distances correspond to roughly 2.1° , 2.7° and 6.2° in great circle distance. Given the colour is often not recorded, we have to assume an altitude and the lowest altitude gives that the same patch of auroral sky is visible over a circle of diameter of order 460 km. To put this in context, we note that London, for example, has an east-west diameter of 58 km and a north-south diameter of 40 km and hence giving the coordinates of the centre of London for any observation described as from “London” is within allowable uncertainties. On the other hand, the country of England has dimensions of about 330 km east-west and 570 km north-south, and hence using the centre location of a sighting labelled as “England” would not cover all locations in England to within an acceptable error. Hence, the central location is acceptable for most major cities and smaller locations, but observations labelled by the name of the country or of a large county, state or region are usually not. Thus, we use the central location for a given definition

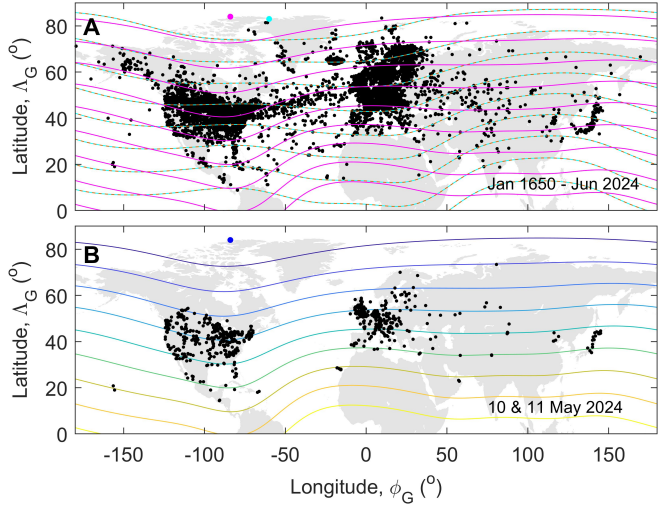


Figure 1. The global distribution of area-combined auroral observations (“samples”) used in this paper. Part **A** is for all of the 191660 area-combined samples from the interval January 1650 to June 2024. The mauve contours are quasi-dipole (QD) geomagnetic latitudes (see section 2.3), Λ_M , of $[0:10^\circ:80^\circ]$ for 2024 and the brown and cyan dashed contours are the same for 1650. The mauve and cyan dots give the corresponding north magnetic pole locations for these years. Part **B** is for the 790 samples on the nights of 10 and 11 May 2024. The coloured contours (yellow to dark blue) are QD geomagnetic latitudes, Λ_M , of $[0:10^\circ:80^\circ]$ for May 2024 and the blue dot is the north magnetic pole location.

of a location but only if all places that could be interpreted under that name are within about 50 km of that central location.

We use the astronomical definition of a “night” which extends for 24 hrs from local midday. However, in many catalogues or reports of observations, no Universal (UT or UTC) nor local time is given, hence one cannot be sure the same definition has been used. As a result, every report date is here treated as having an uncertainty of ± 1 day because observations made after local midnight may have been labelled with either date.

Figure 1 **A** shows a map of the locations of the area-combined observation samples used in this paper for the entire interval (January 1650 to June 2024). The map shows a dearth of observations from Siberia, compared to other areas on the northern-hemisphere land mass and even compared to the North Atlantic, where shipping has provided regular sightings. This is largely a consequence of the low population density in this region. There are catalogues of Siberian auroral observations that have been constructed (e.g., [Ptitsyna & Demina 2021](#)), but these are not available on-line and some need translating from Russian. Future work will extend the survey to try to better fill this longitude gap. More samples have appeared in recent years as auroral tourism to Siberia has increased, but numbers are still low and the number of sites in Siberia from where aurora are recorded is still low. Social media posts from inhabitants tend to be in Russian and many internet posts are in commercial sites selling images which tend to give the locations of auroral images but not the date on which it was recorded. Part **B** of Figure 1 shows the corresponding map for the 790 area-combined samples on 10-11 May 2024 in our database, which came from 1103 reports of sightings (696 of which were from the *Aurorasaurus* and *Skywarden* citizen science projects and were given in the supplementary information files attached to the paper by ([Grandin et al. 2024](#))). The contours are relevant quasi-dipole (QD) geomagnetic latitudes Λ_M (see section 2.3).

In the first hundred years of the survey (1650–1750), there are, on average, just 0.140 samples per night. This figure has risen over time and for 1750–1850 the average is 0.684 per night and for 1850–1950 it is 3.246 per night. For the latest 74.5 years (1950–June 2024) the average has fallen again to 1.546 samples per night, and that has remained roughly constant (for example, for the last 5 years the number is 1.484). Hence, during the 10–11 May 2024 the number of area-averaged reports per night was higher than the recent average for the time by a factor of 266.

2.2 An example of a well-studied storm in the dataset

Figure 2 is an example of the auroral records in a large (but not extreme) auroral event. This is the “St Patrick’s Day” storm that occurred on 17 and 18 March 2015. The interplanetary causes of this storm and some of its effects have been studied by Wu et al. (2016) and by Jacobsen & Andalsvik (2016) and the consequent aurora was studied by Case & MacDonald (2015) from data collected by the *Aurorasaurus* citizen science project. The effect of this storm on the energetic electron population in the outer radiation belt has been studied by Pierrard & Lopez Rosson (2016), as will be discussed further in the next section. The black dots in Panel A show the quasi-dipole (QD) geomagnetic latitudes Λ_M (see Section 2.3) of the area-combined auroral samples in intervals of durations 28 days before and after the main phase of this storm. The light-grey, mid-grey and darker-grey areas delineating Λ_M values that are within, respectively, the $\pm 3\sigma$, $\pm 2\sigma$, and $\pm 1\sigma$ points of the distribution for all area-combined samples in this survey (covering January 1650 to June 2024) and the mean is shown by the mauve line (see Section 3.3). Panel B shows the 3-hourly values of the homogeneous aa_H (Lockwood et al. 2018a,b) in a bar-chart format, where the vertical bars are coloured according to their height. Panel C is the same as B, but for hourly values of the Dcx geomagnetic index. Panel D shows the International sunspot number R , and Panel E shows the area (in millions of a solar hemisphere, μsh) of sunspot groups: the major groups are numbered using the NOAA identification scheme and the yellow dot marks an C9.1/1F-class solar flare that occurred in group 12297 and was associated with the launch of the CME that hit Earth causing the geomagnetic and auroral storm. The vertical dashed lines delineate the intervals used to generate the global precipitation maps in parts A and B of Figure 5. Note that the horizontal axis is in fractional day-of-year, which is zero at 00:00 UTC on 1 January.

Throughout the paper, we use the Dcx index in preference to Dst . Dcx was introduced by Karinen (2005) and has a number of advantages: Dcx extends back to 1932 whereas Dst only extends back to 1957; Dcx is also more homogeneous in its construction and uses better weighting of stations than Dst (Mursula et al. 2011). Like Dst , Dcx is increasingly negative for greater disturbance levels and is strongly modulated by the ring current in Earth’s inner magnetosphere. (However, it is also influenced, to a lesser extent, by the currents that flow in the magnetopause boundary).

The sunspot group areas are retrieved from the excellent Debrecen Photoheliographic Database, maintained by the Heliophysical Observatory. The data have been processed as described by Baranyi et al. (2016) and consistency with the earlier data from the Royal Greenwich Observatory (RGO), which are also available in the same database, has been improved and recalibrated by the work of Györi et al. (2017). There has been discussion about sunspot group area estimates because those from the USAF (United States Air Force) Solar Observing Optical Network (SOON) are consistently lower than obtained from other data and by other methods by of order 25%–50% (Meadows 2020). However, the Debrecen areas agree well with other estimates (e.g. Mandal et al. 2020).

The storm is seen as a very prominent peak in aa_H and an equally clear minimum in Dcx . It can be seen that the aurora moves to just below the 3σ magnetic latitude at the event peak, but most of the time before and after the storm, the aurora is almost always poleward of its mean location and equatorward of the upper 1σ value of the overall Λ_M distribution. In this case, there is a clear location of solar origin with a dominant sunspot group (12297) near the centre of the solar

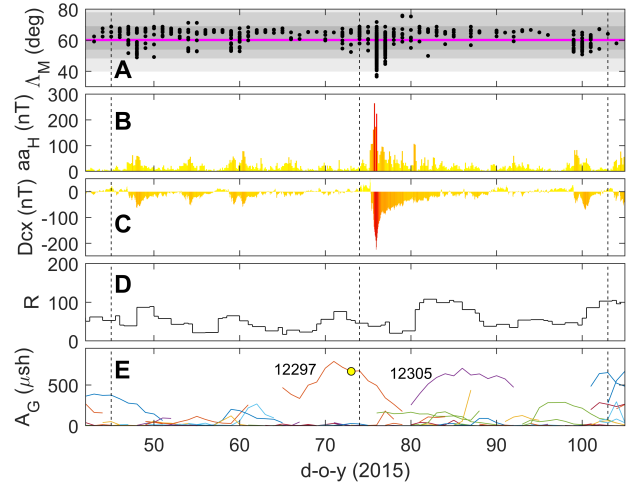


Figure 2. An example of geomagnetic and auroral storm, the “St. Patrick’s Day storm” of 16–18 March 2015. **A** shows the QD geomagnetic latitude Λ_M of samples of area-combined auroral observations. The grey areas delineate values from Λ_M distribution for all the samples in this survey presented in this paper (January 1650–June 2024): the light-grey, mid-grey and darker-grey areas delineating values that are within, respectively, the $\pm 3\sigma$, $\pm 2\sigma$, and $\pm 1\sigma$ points of the distribution, the mean which is shown by the mauve line (see Section 3.3). **B** 3-hourly values of the homogeneous aa_H (Lockwood et al. 2018a,b) in a bar-chart format where the vertical bars are coloured according to their height. **C** The same as **B** for hourly values of the Dcx geomagnetic index. **D** shows the International sunspot number R , and **E** the area (in millions of a solar hemisphere, μsh) of sunspot groups: the major groups are numbered using the NOAA identification scheme and the yellow dot marks an C9.1/1F-class solar flare that occurred in group 12297 and was associated with the launch of the CME that hit Earth causing the geomagnetic and auroral storm. The vertical dashed lines delineate the intervals used to generate the global precipitation maps in parts **A** and **B** of Figure 5. Note that the horizontal axis is in fractional day-of-year, which is zero at 00:00 UTC on 1 January.

disc that gave rise to a C9.1/1F-class flare (Bamba et al. 2019) that was associated with a CME that was observed using the LASCO (Large Angle and Spectrometric Coronagraph Experiment) coronagraph on the SoHO (Solar and Heliospheric Observatory) satellite early in its propagation to Earth and then detected in near-Earth space by the *Wind* spacecraft in orbit around the L1 Lagrange point (Wu et al. 2016).

Figure 3 presents a composite of 13 images of the northern-hemisphere aurora around local midnight during the St Patrick’s Day storm. These are measured by the VIIRS (Visible Infrared Imaging Radiometer Suite) instruments on the Suomi-NPP satellite at visible and near-infra-red wavelengths (500 to 900 nm) (Kalb et al. 2023; Shao et al. 2016). This band covers the primary emission lines of atomic oxygen (green at 557.7 and red at 630) as well as the molecular nitrogen emission lines in the 600–700nm range (blue and violet) that are observed in auroras. The images have been filtered and dynamically scaled using the “ERF-dynamic scaling” procedure, which brings out bright features (without saturating the image) but tends to suppress broad diffuse regions. These images show that, although some ground-based observations of the aurora are within the oval, as imaged from space in this way, many of the ground-based observations, at all longitudes, appear in the region of considerably lower intensity, equatorward of the main oval. Note also that time development of the auroral emission aliases with the observation intervals, sometimes giving sharp boundaries between the images.

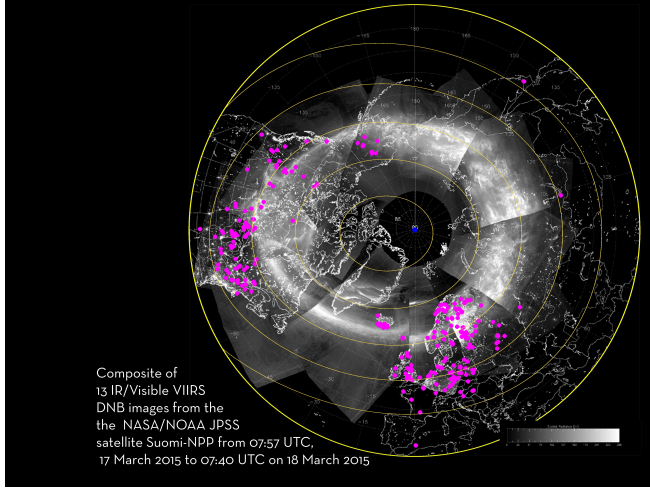


Figure 3. A composite of 13 DNB (Day/Night Band) Images from the VIIRS (Visible Infrared Imaging Radiometer Suite) instrument on the Suomi-NPP (Suomi National Polar-orbiting Partnership) satellite, a joint NOAA/NASA mission. These were recorded between 07:57 UT on 17 March 2015 and 07:40 UT on 18 March 2015 during the St. Patrick’s Day storm and were filtered and scaled using the “ERF-dynamic scaling” algorithm and provided by Curtis Seaman (<https://rammb.cira.colostate.edu/projects/npp/blog/index.php/uncategorized/the-aurora-seen-around-the-world/>). The mauve dots are locations from which aurora was reported from the ground on 17 and 18 March 2015 and the orange contours are QD geomagnetic latitudes, Λ_M , of $[40^\circ:10^\circ:80^\circ]$ for the date in question. The yellow circle is at geographic latitude $\Lambda_G = 35^\circ$ and the blue dot is the geographic pole ($\Lambda_G = 90^\circ$). Auroral images are courtesy of the VIIRS Imagery and Visualization Team, CIRA, Colorado State University, USA.

We have also generated the equivalent to Figure 3 using image swaths observed on the same night by the Special Sensor Ultraviolet Spectrographic Imager (SSUSI) far ultraviolet (FUV) imagers on the Defense Meteorological Satellite Program (DMSP) F18 satellite (not shown). The same feature of many ground-based observations being equatorward of the main oval seen from space is noted, but it is to a lesser extent than in Figure 3: this is because the auroral oval seen in the FUV images reaches somewhat lower latitudes than is seen in the IR/Visible images. We note that Kosar et al. (2018) used DMSP-SSUSI data to compare the auroral oval boundaries at local midnight during the St Patrick’s Day storm, as derived from the ground-based and by DMSP/SSUSI observations. They found an agreement, but it was not a close agreement. There are a number of reasons why auroras can be seen on the ground when it is not seen from space. One is temporal variations, because the relevant part of the satellite image is not, in general, recorded at the same time as the ground-based observations. The second is intensity levels: broad diffuse emission regions tend to be lost in space-based images when filtering and image-processing is aimed at highlighting the bright discrete structures in the presence of a large dynamic range of emission intensity.

2.3 Choice of the definition of geomagnetic latitude

There are a number of geomagnetic latitude estimates used in studies of solar-terrestrial science, and there are differences between them. Each has its particular strengths and weaknesses in relation to a given application. These include dip latitude, apex latitude, modified apex

latitude, invariant latitude, corrected geomagnetic latitude (CGM), PACE coordinate latitude, constant B-Minimum coordinate latitude; Altitude-Adjusted Corrected Geomagnetic (AACGM) latitude and QD latitude (Richmond 1995; Shepherd 2014; Laundal & Richmond 2017).

All these magnetic latitudes for a given geographic location are computed using a model of the geomagnetic field. In the present study, we use the thirteenth generation IGRF (International Geomagnetic Reference Field) for 1900 to 2025 (Alken et al. 2021) and the gufm1 model for before 1900 (Jackson et al. 2000).

For auroral studies (e.g. Lockwood & Barnard 2015; Kataoka & Nakano 2021), dip geomagnetic latitudes have sometimes been used. These are given by a simple relation to the inclination of the field at Earth’s surface (the angle of the field with respect to the vertical), I

$$\Lambda_D = \tan^{-1} \left(\frac{\tan(I)}{2} \right) \quad (1)$$

This has often been used in historical studies of aurora (e.g. Lockwood & Barnard 2015), because of the ease of splining together values from models of the field used to compute the I values in different epochs. In addition, the differences between Λ_D , as defined by Equation 1 and other magnetic latitude estimates stay relatively constant for a limited region of study. However, other studies have found that other geomagnetic latitudes better describe auroral morphology (e.g. Kataoka & Nakano 2021).

Magnetic Apex coordinates are calculated by tracing along magnetic field lines of the magnetic field model (in this case IGRF but splined to values from gufm1 for before 1900), from the point in question, P , to the highest point above the Earth (the apex) allowing for the deformation of the Earth’s surface from a spherical form. The field line apex is at a geodetic height of h_a and the point in question is at a geodetic height of h . The Modified Apex (MA) latitude, Λ_A , is defined relative to a constant reference height h_r by

$$\Lambda_A = \pm \cos^{-1} \left(\frac{R_E + h_r}{R_E + h_a} \right)^{1/2} \quad (2)$$

where R_E is the mean radius of the Earth. The sign is positive in the Northern magnetic hemisphere and negative for the Southern. The quasi-dipole (QD) latitude is very similar to Λ_A but is defined relative to the geodetic height of the point P , h_p .

$$\Lambda_M = \pm \cos^{-1} \left(\frac{R_E + h_p}{R_E + h_a} \right)^{1/2} \quad (3)$$

hence MA and QD latitudes are very similar; however, MA latitudes do not depend on the height of the point P (being referred to a constant altitude, h_r). For $h_r = h_p$ the two are the same but diverge if $h_r > h_p$. QD coordinates are useful for phenomena with a specific height profile because they allow for h_p and do not depend on a defined reference height. Reviews of MA and QD coordinates have been given by Richmond (1995) and Laundal & Richmond (2017).

Figure 4 compares maps of dip Λ_D and QD Λ_M latitudes for an example year of 2015. It can be seen that the two are very similar at equatorial latitudes (values between -20° and $+20^\circ$) but the differences grow at higher latitudes. These differences are particularly severe in the Southern Hemisphere, where the South Atlantic Anomaly (SAA) generates a large feature in Λ_D that is absent in Λ_M .

In this paper, we use QD latitudes Λ_M based on a join of magnetic field models IGRF and gufm1 in the following manner. We zero pad the IGRF spherical harmonic coefficients to match the maximum

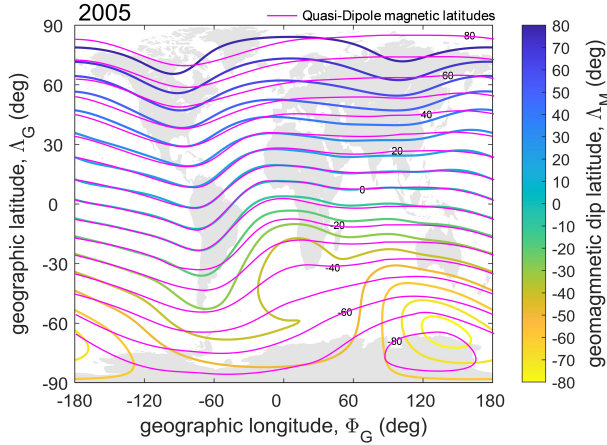


Figure 4. A comparison of dip geomagnetic latitudes Λ_D and QD geomagnetic latitudes Λ_M for an example year (2015). Contours, 10° apart, are shown of Λ_M (in mauve) and Λ_D (coloured according to the scale) on a Mercator map projection (as a function of geographic longitude Φ_G and latitude Λ_G)

spherical harmonic degree (14) of gufm1, and then linearly taper the coefficients of gufm1 for 1890 to 1900 to those of IGRF at 1900 to prevent a step change in their values at the join. We then sample these combined model coefficients at the appropriate times to rebuild the cubic spline time basis of gufm1, ensuring that the linear time variation of IGRF is still retained after 1900. We compute Λ_M values using this field model with a modified version of the “apexp” software (van der Meeren et al. 2023; Emmert et al. 2010).

That Λ_M orders particle precipitation more accurately than Λ_D is demonstrated by Figure 5 which compares contours of Λ_M with energetic electron precipitation observed by the PROBA-V spacecraft at an altitude of 830 km. These electrons are in the energy range 0.5–0.6 MeV which means they were trapped particles in the outer radiation belt and ring current that have been scattered into the loss cone. Parts A and B of Figure 5 are global maps derived over periods of 28 days immediately before and after the St. Patrick’s Day storm presented in Figures 2 and 3. Antonova et al. (2018) argue that the auroral oval maps to the outer ring current and the outer part of the outer radiation belt, rather than the plasma sheet as often assumed. That is consistent with Figure 5, in that 95.4 % of all the auroral observations used in this paper are between the two mauve lines shown. In addition, the black points show the locations of the auroral samples in the interval over which each precipitation map was compiled. Parts A and B are for, respectively, before and after the St Patrick’s day storm and the increase in particle fluxes caused by the storm is apparent, as is the equatorward expansion of the aurora. Both parts show a major feature in the SAA, where particles precipitate because the loss cone width in pitch angle is increased by the low field strengths. These electrons are considerably more energetic (by a factor of order 50) than those that excite most auroras, which are typically in the 1–10 keV range. However, being so energetic means that their trajectories are close to field-aligned (field perpendicular convection during flight times is negligible) and we can see that at auroral latitudes they are well-ordered by the Λ_M contours. Studies using lower-energy electrons show that these auroral bands of high energy electrons coincide closely with the locations of auroral electron precipitation seen by the DMSP (Defense Meteorological Satellite Program) satellites at similar altitudes (Liu et al. 2024). Liu

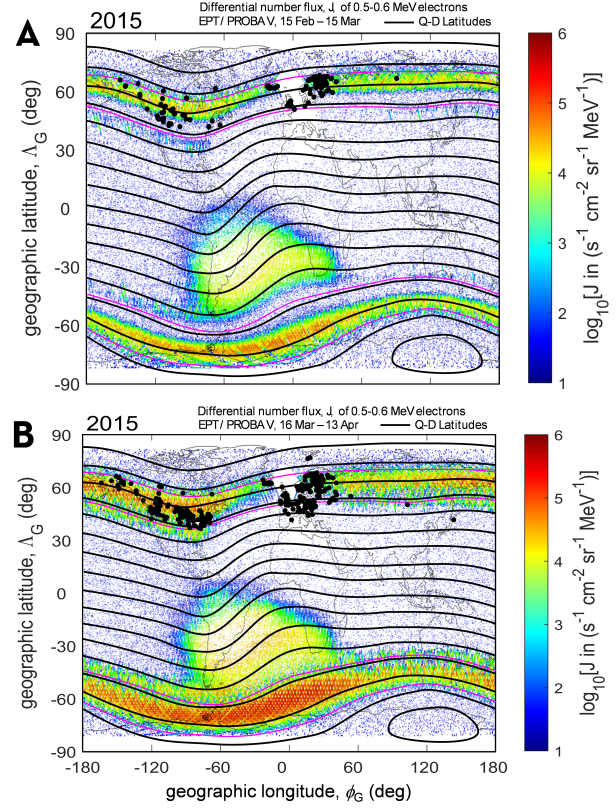


Figure 5. Ordering of particle precipitation by QD latitude, Λ_M . Contours of Λ_M for 2015 are shown in black as a function of geographic longitude ϕ_G and latitude Λ_G . The coloured pixels give the differential number flux, J , of precipitating electrons in the energy range 0.5–0.6 MeV, as detected by the Energetic Particle Telescope (EPT) on the PROBA-V satellite (Cynamukungu et al. 2014) over the intervals A 15 Feb – 15 Mar 2015 and B 16 Mar – 13 Apr (Pierrard & Lopez Rosson 2016) which are, respectively, before and after the “St Patrick’s Day” geomagnetic storm. The mauve contours are the 2σ points of the total distribution of Λ_M values of auroral observations derived from the catalogue of northern-hemisphere observations for 1650–2024 used in this paper. The black dots are area-combined samples of auroral observations in the same interval as used to compile the map of electron precipitation.

et al. (2024) also identify the auroral oval from 3 years’ data on high frequency magnetic fluctuations detected by AC Vector Magnetometer (ACMag) instrument on the Fengyun-3E satellite and show it to be in the same location as the energetic electron precipitation and auroral observations shown in Figure 5.

The orange lines in Figure 3 are contours of constant Λ_M and show that during the St. Patrick’s Day event, the aurora observed in the VIIRS DNB images are largely between $\Lambda_M = 60^\circ$ and $\Lambda_M = 70^\circ$. This shows that Λ_M is effective in ordering the aurora, but we need to remember that the composite of images was taken over an extended interval of about 24 hours at the peak of the storm. Hence, variations in the latitude of the aurora with time will appear as longitudinal variations in the image composite. Figure 2B shows that the peak in mid-latitude aa_H index during the storm was at 18:00 UTC on 17 March 2015. Part C shows that the peak of the storm in the ring current (the minimum in the D_{cx} index) was later at 23 UTC, as expected for the ring current growth time. The image in the composite shown in Figure 6 recorded at 18:00 UT is that over mid-Siberia, in which aurora extends down to near $\Lambda_M = 52^\circ$ in the image and mid-

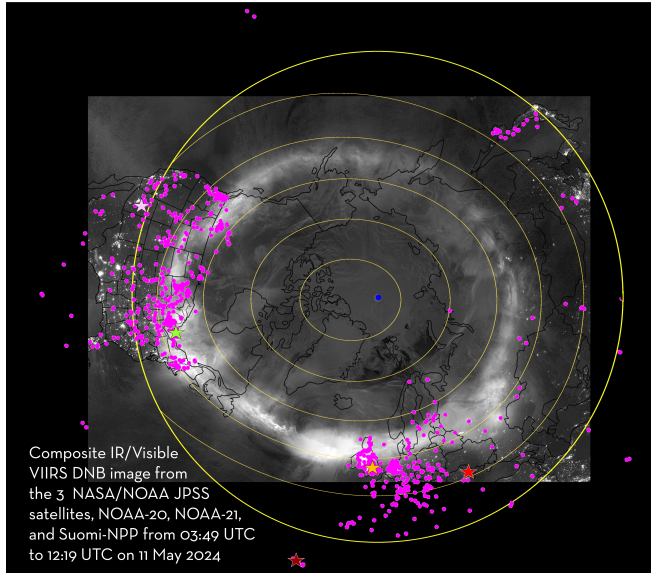


Figure 6. Area-combined auroral samples (mauve points) mapped onto a composite Near-IR/Visible DNB image for the Northern Hemisphere auroral oval during the 10–11 May 2024 Event. This composite is made from images from 3 satellites (unlike Figure 3 which is made from just one): the NOAA/NASA JPSS satellites, NOAA-20, NOAA-21, and Suomi-NPP. The mauve dots are locations from which aurora was reported from the ground on 10 and 11 May 2024 and the orange contours are QD geomagnetic latitudes, Λ_M , of $[40^\circ:10^\circ:80^\circ]$ for that date. The yellow circle is at geographic latitude $\Lambda_G = 35^\circ$ and enables comparison with Figure 3. The coloured stars are the locations from where the images shown in Figure 7 were recorded. Image courtesy the VIIRS Imagery and Visualization Team, CIRA, Colorado State University, USA.

latitude aurora was recorded at this time at about 3° equatorward of this point at the ISTP SB RAS Geophysical Observatory (GPhO), slightly west of Irkutsk (Mikhalev 2019).

3 OBSERVATIONS

3.1 The major auroral event of 10-11 May 2024

Figure 1 **B** shows a map of the locations of the 790 area-combined observation samples for the nights of 10 and 11 March 2024. Like part A of the Figure, the distribution shows a dearth of observations in Siberia. At all longitudes ϕ_G , the range of geographic latitudes Λ_G is increased in Figure 1 **A** by the secular changes in the geomagnetic field which alters the geomagnetic latitude at Λ_M at given geographic coordinates (Λ_G, ϕ_G) as well as by the greater range of geomagnetic activity levels. Nevertheless, an obvious feature is that middle and lower auroral latitudes seen in **A** are present in **B** but the higher latitude observations seen in **A** are missing in **B**. Specifically, in both panels there are observations from the shores and islands of the Caribbean, USA, southern Canada, the UK, Central Europe, Southern Fennoscandia and Japan. However, observations from Alaska, northern Canada, Greenland, Iceland, Faroes, and northern Fennoscandia that are present in part **A** are not seen in **B**.

Figure 6 shows a composite of VIIRS DNB images during the May 2024 storm. Because this composite is taken from identical instruments on 3 satellites (compared to the one used to make Figure 3) it was compiled over a shorter interval of 8.5 hrs and there is not a simple aliasing of temporal variations with longitude. The aurora

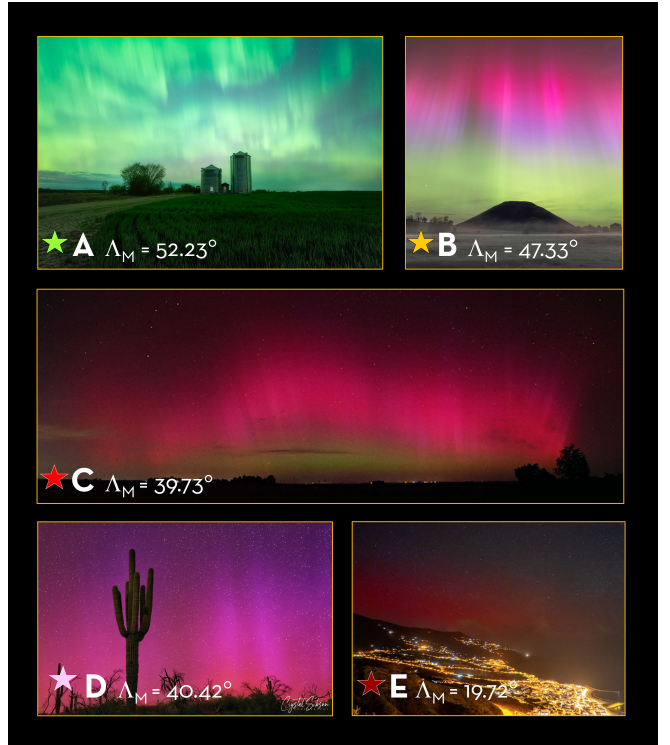


Figure 7. Images from the night of 10–11 May 2024 from the locations marked by coloured stars in Figure 6. **A** predominantly green aurora photographed from Barrie, Ontario, Canada (coordinates $\Lambda_G = 44.38^\circ$ N, $\phi_G = -79.7^\circ$ E - a QD magnetic latitude of $\Lambda_M = 53.23^\circ$). Image credit: Will Dunn, copyright WD Photography. **B** green, blue and red aurora above Silbury Hill prehistoric mound, Wiltshire, England ($\Lambda_G = 51.42^\circ$ N, $\phi_G = -1.86^\circ$ E, $\Lambda_M = 47.33^\circ$). Image credit: Nick Bull, copyright: Stonehenge Dronescapes. **C** panoramic view of predominantly red aurora with a thin, low-altitude band of green, seen from Fundulea, Romania ($\Lambda_G = 44.47^\circ$ N, $\phi_G = 26.51^\circ$ E, $\Lambda_M = 39.73^\circ$). Image credit Maximilian Teodorescu, copyright Maximus Photography, Romania. **D** red and blue aurora mixture recorded in the Superstition Mountains, Arizona, USA ($\Lambda_G = 33.48^\circ$ N, $\phi_G = -111.46^\circ$ E, $\Lambda_M = 40.47^\circ$). Image credit: Crystal Sibson copyright Crystal Sibson Photography. **E** red aurora seen at low elevations to the north from Breña Alta, looking over Santa Cruz de La Palma ($\Lambda_G = 28.68^\circ$ N, $\phi_G = -17.78^\circ$ E, $\Lambda_M = 19.72^\circ$). Image credit and copyright: Giovanni Tessicini. All images reproduced with kind permission of the photographers.

is again well-ordered by Λ_M and sits between $\Lambda_M = 50^\circ$ and 60° , which is consistently 10° equatorward of the aurora during the St Patrick's Day storm. As for the St Patrick's Day storm, there are very few ground-based observations poleward of the main oval seen by VIIRS-DNB, some within that oval and many equatorward of it.

Figure 7 shows five typical auroras seen on 10 May 2024 (when not an overhead coronal form). Their locations are marked by stars in Figure 6, using the same identifying colours as in 7. Part **A** is an example of a full sky of green emission and is within the bright auroral band identified in the composite JPSS/VIIRS image. **B** is a clear example of the red emission from above the green. Between them there is blue visible which is an emission from molecular nitrogen and may also be present at the same elevations as the red emission, giving a mauve tint to the red. This image was taken from the equatorward edge of the bright auroral band in the composite JPSS/VIIRS image. It is also taken very close to the geomagnetic latitude above which Grandin et al. (2024) found predominantly green and predominantly red were reported with roughly equal frequency,

but below which predominantly red dominated the reports. The green just can be seen in **C** at the lowest altitudes but not in **D** which are from very similar magnetic latitudes considerably below that of the bright auroral band in the composite JPSS/VIIRS image. Time-lapse movies and sequences of stills from these latitudes on this night show that this faint green lower edge to the red aurora forms and fades quite rapidly and so this difference between these two images is more to do with temporal fluctuations than latitudinal structure. Lastly, **E** is from the Canary Islands and so is very close indeed to the lowest magnetic latitude observation on this day. If any green were present it was below the northern horizon and a red glow is seen to the north at low elevations. Part **E**, and to a lesser extent **C** show a more monochromatic red than **D** which shows a more mauve colour with larger associated emission of blue, which is particularly evident at the higher altitudes. However, in these cases one generally does not know the camera and image colour filters applied; hence such comparisons cannot be rigorous.

3.2 History of major auroral events

Figure 8 shows the history of major events by plotting in Part **A** the geomagnetic latitude Λ_M as a function of date. The grey and white vertical bands mark even- and odd-numbered sunspot cycles, separated by vertical cyan lines at sunspot minima. The sunspot numbers are shown in Part **B**. Because of the secular change in the geomagnetic field, the Λ_M of specific sites have changed. These variations are plotted for a few selected sites to demonstrate the effects. Dashed lines are for sites in the USA/Canada/West-Greenland “American” longitude sector, whereas solid lines are sites at longitudes further east in the “Eurasian” sector. The sites in the American sector have generally migrated poleward in geomagnetic latitude, whereas those in the Eurasian sector have generally migrated equatorward. The sites are named to the right of part **A**.

Note that there are some early, isolated reports of aurora at low latitudes that are not included in Figure 8. These are often based on ambiguously-worded texts and of uncertain provenance. To eliminate these, we do not include reports if there are no other reports on the same night at latitudes below the 1σ point of the distribution of Λ_M values (discussed in Section 2.3). There are also some later low-latitude reports of “aurora” in newspapers that are not included because they almost certainly originated from reports of disruption to telegraph systems. These are discussed in relation to the specific events studied in Section 3.4.

The May 2024 even is at the right-hand edge of the plot and the left-hand edge of the plot is during the Maunder minimum when observations were few and at higher Λ_M values. The Dalton minimum (c.1800-1825) has a clear signature with fewer auroral observations, especially at lower magnetic latitudes. (Indeed, this solar minimum is so-named as it was first noted by John Dalton in his auroral observations). The weaker grand solar minimum around 1900 is also accompanied by fewer observations at lower latitudes.

In addition to these minima, there is a general trend to lower latitudes as sunspot numbers increase through the period. However, it is hard to discriminate between the effects of solar variability and of the magnetic latitudes variations of locations with a population able and willing to record auroral observations. Eurasian observations are present throughout the interval, and European centres of population have migrated to lower latitudes: this is a big factor in the change seen in Figure 8. Observers in the American sector have been moved in the opposite direction in magnetic latitude by the change in the geomagnetic field but there are big changes in the numbers and distribution of potential observers. The Mayflower arrived in America in 1620 and

the first auroral observation in our database is from 1715 in the New England area (Boston). Subsequently, that region moved to higher geomagnetic latitudes and the effect of that is clear in the data and the (magnetic) latitudinal width of the region of observations spread with increased population numbers (of individuals likely to record and aurora). That spread was largely to higher magnetic latitudes (i.e. up into Canada) and observations from the southern American states remained sporadic until about 1900 when the latitude spread suddenly spread reached modern values, probably due to the establishment of the US national weather service in 1870 and the rapid growth of telegraph systems over the interval 1844-1900.

There are other changes to note. Observations in the American sector dropped dramatically after 1950 and only recovered with the growth of the internet, and the effect of that can be seen in Figure 8. In this paper, we are concerned with extreme excursions of the aurora to low latitudes, and not the average location of aurora. Nevertheless, that we have observations from all longitudes is important because not all events are global in their greatest latitude extent. For example, the Carrington event aurora of 1859 was seen down to Λ_M of 16.68° in the American sector but only 23.75° in the European sector. What is interesting is that this event was recorded from almost all latitudes in both continents, even though routine observations were only made at a few geophysical observatories north of Λ_M of about 60° at that time.

Another important point to note in Figure 8 is the onset of auroral observations at a few sites at very high magnetic latitudes starting around 1850. These sites are on the west coast of Greenland and are observatory stations that provided regular data. (The selected station of Upernivik is mid-way along the west coast of Greenland). These data come from the collection of Sam Silverman, and our data ceases at the end of his dataset. There are two points to note. Firstly, there would be an almost continuous latitudinal distribution of observations if there were European or American scale population density on Greenland. Secondly, the monitoring of even a few sites at those magnetic latitudes has been sporadic. Hence, although our survey can tell us something about the variability of auroral occurrence at lower latitudes (Λ_M below about 60°), it gives us almost no usable information about the long-term behaviour of aurora poleward of that.

Figure 9 is the same as Figure 8, but expanded to cover just the modern era (January 2013-June 2024). The intervals cover the peaks of cycles 24 and 25 and the minimum between them, as shown by the lower panel, part **B**. Panel **A** reveals the annual variation in samples that we expect because of the effect of sunlight on the day side of the Earth. The solid vertical blue lines have been added to mark the summer solstice for these northern-hemisphere data, and the vertical blue dashed lines mark the winter solstice. The expected annual variation is present, with a clear minimum in occurrence around the summer solstices, particularly at higher latitudes. There is also a clear semi-annual variation, with peak occurrence being at the equinoxes.

The semiannual variations in geomagnetic activity are well understood in terms of the dipole tilt effect on solar-wind magnetosphere coupling, known as the Russell-McPherron effect (Russell & McPherron 1973). A variety of tests have shown conclusively that this is the causal mechanism, one of the most compelling being that the favoured equinox depends on the polarity of the Y-component of the interplanetary magnetic field (IMF), which is an unique prediction of the Russell-McPherron theory (Zhao & Zong 2012; Lockwood et al. 2020a,b,c).

Figure 10 shows the semi-annual variations in the number of samples at geomagnetic latitudes below 5 different thresholds for the whole dataset (January 1650-July 2024). All show clear peaks

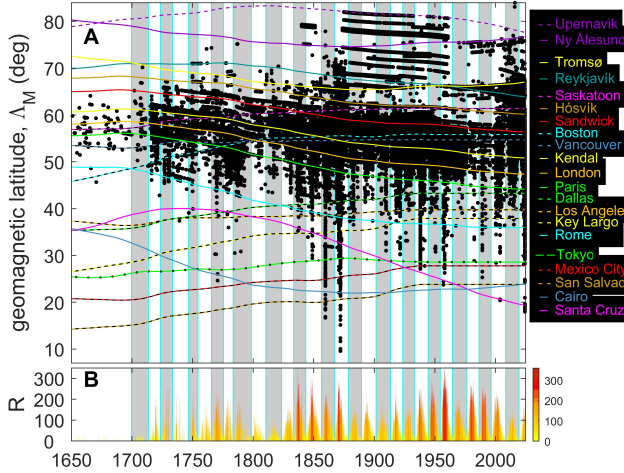


Figure 8. **A** A plot of the locations on a QD geomagnetic latitude (Λ_M) as a function of time for 190953 independent samples from 216321 observation records taken over the interval January 1650–June 2024. Vertical cyan lines mark sunspot minima and grey and white shading denotes, respectively, even- and odd-numbered sunspot cycles. The various coloured lines give the variation of Λ_M with time for several selected sites (named on the right-hand side), computed from the spline of gufm1 and IGRF geomagnetic field models. **B** Carrington rotation means of sunspot number, R shown in a bar-chart format where the histogram bars are coloured according to their height.

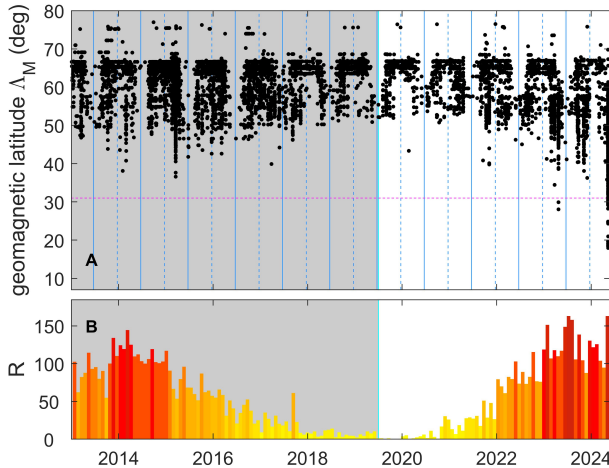


Figure 9. Same as Figure 8 but for the interval January 2013 to June 2024, covering approximately one solar cycle. In part A vertical solid and dashed blue lines have been added marking, respectively, the June and December solstices and a mauve horizontal dashed line marking the 31° -threshold for an extreme event that is adopted here

around the March and September equinoxes. In all cases, the March equinox peak is slightly lower and broader than the September one. For the 90° threshold (all samples) there are fewer samples around the June solstice than the December solstice, as expected because of the reduced opportunity to observe aurorae caused by daylight. This difference decays with the latitude threshold and is negligible at 50° and lower. This behaviour can also be identified in the annual variations visible in Figure 9. We conclude that the annual variation

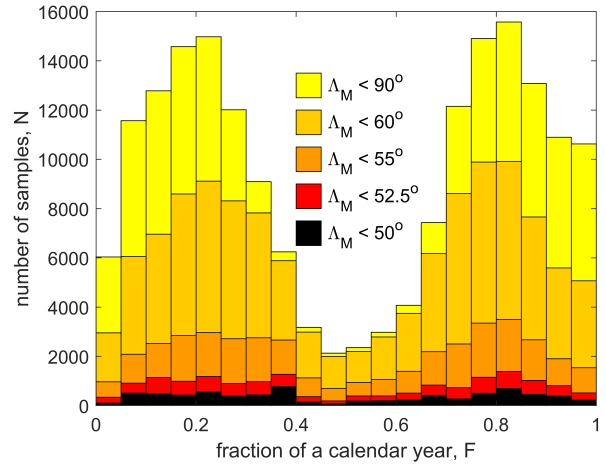


Figure 10. Histograms of annual numbers of samples in bins of a fraction of a year F that are 0.05 wide. The shading from yellow to black is for samples with $\Lambda_M < 90^\circ$ (i.e., all samples), $\Lambda_M < 60^\circ$, $\Lambda_M < 55^\circ$, $\Lambda_M < 52.5^\circ$ and $\Lambda_M < 50^\circ$

due to the axial tilt of the Earth does not influence the auroral occurrence at magnetic latitudes below about 50° . Figure 6 of Lockwood et al. (2020a) shows there is very little difference in the occurrence of large geomagnetic disturbances at the solstices, as is found here for auroral disturbances that reach to magnetic latitudes below 50° . More detailed comparison of the semi-annual variations in auroral and geomagnetic activity will be presented in a later paper.

3.3 The distribution of geomagnetic latitudes of auroral events

Figure 11A is a histogram of the distribution of the geomagnetic QD latitudes of auroral sightings, Λ_M , for the entire 374.5-year period (January 1650–July 2024). The solid vertical mauve lines give the 2σ points of the distribution (i.e., the 2.5 and 97.5 percentiles), which were plotted on the world maps (in both hemispheres) in Figure 5.

It can be seen that above the mode value the distribution is not smooth, this is expected because of the observations at the highest latitudes are from regions of very low population density and largely come from a few research station sites. In addition, the intervals covered by these observations are short and data from summer months are almost entirely missing because of sunlight. The data that are available suggest the distribution is rather asymmetric, with the mode at a considerably lower value than the mean and the latitudinal width above the mode value being considerably greater than below the mode.

However, these problems are much greater at the high latitudes because below the mode value the latitudinal distribution of potential observers is essentially continuous. Here the distribution is relatively smooth. Part B of Figure 11 is a detail of the low latitude tail of the distribution. The small number of the samples in this extreme tail of the distribution mean that the uneven geographic distribution of potential observers is having an effect. However, below a marked peak at $\Lambda_M = 31^\circ$ the distribution is close to an exponential in form. This is demonstrated by the orange line in B which is the best-fit exponential to values at $\Lambda_M < 45^\circ$, given by $ae^{(b\Lambda_M)}$ where $a = 0.045$ and $b = 0.216$. Part C and D are the cumulative distribution functions (CDF) for the same data as in A and B, respectively.

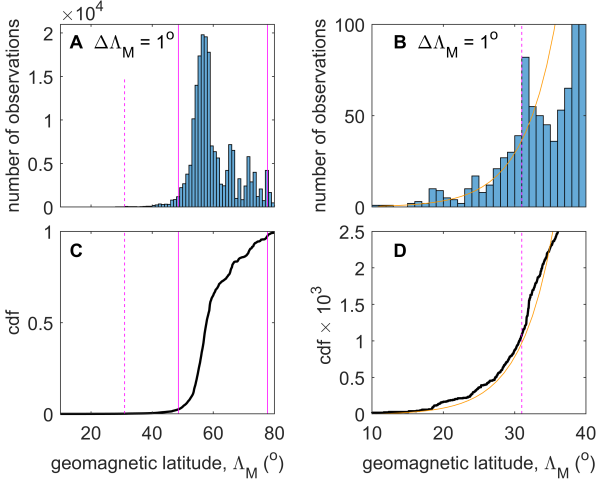


Figure 11. Distributions of the number of area-combined samples, N with QD geomagnetic latitude, Λ_M . **A** is a histogram of the full distribution in bins of $\Delta\Lambda_M = 1^\circ$ degree wide. **B** Detail of the low-latitude tail of the distribution shown in **A** with the orange line being the best-fit exponential rise of the distribution at $\Lambda_M < 45^\circ$ which is given by $a e^{(b\Lambda_M)}$ where $a = 0.045$ and $b = 0.216$. Part **C** is the cummulative distribution function (CDF) corresponding to **A**: the solid vertical mauve lines are the 2σ points of the distribution. Part **D** is the CDF corresponding to **B**: the vertical dashed line in all plots is at $\Lambda_M = 31^\circ$ and marks the point where the distribution departs from the exponential. This is taken in this paper to be the threshold latitude for an extreme event. The CDF at this threshold is equal to 5.0×10^{-4} and hence below this latitude are just 0.05% of auroral sightings. The median auroral latitude is 57.023° and the 2σ range is 48.7 to 71.2° .

We are interested in the present paper in excursions of aurora to low latitudes. The mode of the distribution in Figure 11A is 57.50° and the mean is 59.45° . The 1σ , 2σ , and 3σ , points of the distribution equatorward of the mean are 54.45° , 48.72° , and 40.78° , respectively. As the distribution of Λ_M values below 31° is close to an exponential in form, and so seemingly not greatly influenced by the geographic distribution of potential observers, we here define this geomagnetic latitude to be the low-latitude threshold to define an extreme event. This threshold is shown by the vertical dashed mauve lines in Figure 11 and the area-combined samples at Λ_M below this threshold are just 0.05% of the total dataset.

Figure 12 plots as black dots on a northern-hemisphere map where extremely low-latitude auroral sightings have been made since 1650. Part A shows all observation locations where $\Lambda_M \leq 31^\circ$. On the map are also plotted the $\Lambda_M = 31^\circ$ contours for years 50 years apart between 1650 and 2000. In Part B the observation locations just poleward of the $\Lambda_M = 31^\circ$ contour are plotted on a map of the population density in the year 2022. This population map will obviously have changed considerably over the years, in particular with increasing numbers of individuals per unit area, but also with some spread in the locations where significant numbers of people live. However, a modern map is sufficient for our purposes. Both panels show that there is a clear correlation between where people live and where these extremely low-latitude aurora were observed. However, in Part B it can be seen that many of the observations just poleward of $\Lambda_M = 31^\circ$ threshold are on the northern edge of a region of little-to-no population, in particular the Gobi Desert in China, the Sahara desert in Africa and the South Caribbean Sea between Cuba and Jamaica and the continent of South America. In addition, several of these locations also have a clear northern boundary, for

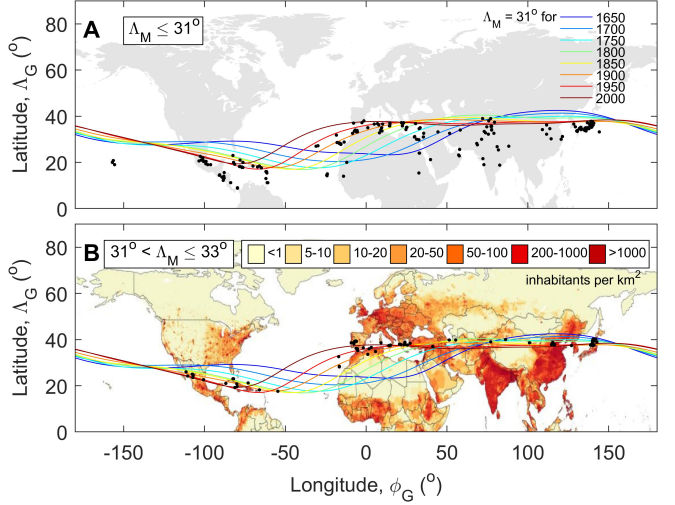


Figure 12. Maps of **A** locations of observations at geomagnetic QD latitudes below 31° (black points) and **B** of observations at low latitudes that do not quite meet the $\Lambda_M \leq 31^\circ$ criterion, being at $31^\circ < \Lambda_M \leq 33^\circ$. The coloured contours on both panels are of $\Lambda_M = 31^\circ$ for the years of [1650:50:2000]. The map in Panel **B** shows the global population density (in individuals per km^2) in modern times (2022) (Mathieu & Rodés-Guirao 2022).

example Cuba, Jamaica, the Mediterranean coast of North Africa and Turkey. In addition, there are areas that extend to latitudes below $\Lambda_M = 31^\circ$ that have a clear northern boundary (for example, the east China/Mongolia border and middle Mexico). Hence, the peak in the number of area-combined samples of observations between Λ_M of 31° and 32° in Figure 11B is understandable in terms of the population distribution just poleward of the threshold.

In Part A of Figure 12 we can see that the locations where observations were made south of $\Lambda_M = 31^\circ$, and Part B shows the locations are all where high population density extends south to lower latitudes. Hence, the extreme low-latitude events with $\Lambda_M \leq 31^\circ$ were seen in high population areas such as (from east to west) as Japan; eastern China; two small sub-Himalayan regions near $77^\circ E$ that include Xinjiang province in western China, Ladakh and Kashmir in India and northern Pakistan; the Middle East; the north-west coast of Africa and the Canary Islands; and Mexico and Central America.

The evolution of the $\Lambda_M = 31^\circ$ contour with year is interesting because the biggest changes are over the Sahara and the middle Atlantic Ocean where population numbers are small or zero and so these changes make almost no difference to the probability of observing aurora. The main place where the secular change in the geomagnetic field may have altered the relationship of our threshold contour with population density is the Middle East and Arabia, where both population numbers and auroral observations are both quite low and spread thinly. Hence, our choice of threshold also means that the secular change in the magnetic field has had a relatively minimal effect on the general probability of observation of very low-latitude aurora.

Table 1. Great auroral events, ranked by the lowest QD geomagnetic latitude, Δ_M , from which aurora was observed. Columns from left to right give: 1. The rank. 2. Date. 3. The minimum Δ_M at which aurora was observed. 4. The number of area-combined samples N on that date with $\Delta_M < 31^\circ$. 5. The separation in magnetic latitude of the lowest two Δ_M sample sites on that night $\Delta\Delta_M$. 6. the site of the minimum Δ_M observation. 7. The minimum value of the D_{cx} index during the associated geomagnetic storm (values in square brackets are estimates of Dst for events for which no D_{cx} value is available and “n.a.” stands for “none available” and means neither a D_{cx} value nor a Dst value that is independent of Λ_M is available). 8. The peak aa_H index value in the event. 9. A note or name by which the event is often referred to. 9. Literature reference(s) that discuss the event.

1 rank	2 date	3 minimum Δ_M	4 N $\Delta_M < 31^\circ$	5 $\Delta\Delta_M$ ($^\circ$)	6 site of minimum Δ_M	7 minimum D_{cx} (nT)	8 maximum aa_H (nT)	9 Note	10 Refs.
1	04-Feb-1872	9.71	52	0.46	Mumbai, India	[n.a.]	626	Secchi event	Berrilli & Giovannelli (2022) , Silverman (2008) Hayakawa et al. (2023b) , Hayakawa et al. (2018a)
2	28-Aug-1859	16.68	5	0.22	Panama & ship ‘Sarnac’	[950±115]	n.a.	Precursor to Carrington event	Green & Boardsen (2006)
3	11-May-2024	18.08	12	0.43	Ad Dakhiliyah, Oman	-390	521	May 2024 event, day 2	Hayakawa et al. (2024)
4	02-Sep-1859	18.40	24	0.20	La Unión & ships ‘Sabine’ & ‘St Mary’s’	[950±115]	n.a.	Carrington event – day 2	Silverman (2006) , Hayakawa et al. (2018b) Green & Boardsen (2006) González-Esparza & Cuevas-Cardona (2018)
5	01-Sep-1859	18.60	14	5.14	ship ‘St Mary’s’ (off El Salvador coast)	[950±115]	n.a.	Carrington event – day 1	Silverman (2006) , Hayakawa et al. (2018b) Green & Boardsen (2006)
6	10-May-2024	19.12	16	0.58	Mogán, Gran Canaria	-390 (0.0031%)	521	May 2024 event, day 1	Hayakawa et al. (2024)
7	20-Nov-2003	20.41	4	0.22	Mount Teide, Tenerife	-418 (0.0021%)	564	1CR after Halloween storms	Vázquez & Vaquero (2010)
8	24-Oct-1870	22.03	9	2.14	Giza,Cairo,Egypt	[n.a.]	368		
9	21-Jan-1957	23.73	2	0.68	Arrecife, Lanzarote & Gran Canaria	-255 (0.0641%)	416	IGY January storm	Vázquez & Vaquero (2010) , Hayakawa et al. (2023a)
10	5-Feb-1872	24.08	1	8.38	Shaoxing, Zhejiang,China	[n.a.]	626	Day after the Secchi Event	
11	13-Mar-1989	25.30	3	1.24	Dominica & Honduras	-564 (0%)	722	Quebec power outage storm	Boteler (2019) , Allen et al. (1989)
12	11-Feb-1958	26.28	8	0.93	Origi,Japan	-421 (0.0017%)	503	IGY storm	Hayakawa et al. (2023a)
13	25-Jan-1938	26.48	21	0.73	Tataouine, Tunisia	-336 (0.0090%)	656	the Fátima Storm	Hayakawa et al. (2021)
14	18-Sep-1941	27.75	1	5.44	Tunis, Tunisia	-404 (0.0026%)	459	the “geomagnetic blitz”	Love & Coïsson (2016) , McNish (1941)
15	23-Apr-2023	28.05	2	1.86	Hanle, Ladakh,India	-208 (0.0828%)	205		Vichare et al. (2024)
16	14-Jul-2000	28.20	4	0.05	Mexico City	-295 (0.0197%)	352	The Bastille storm	Kubota et al. (2017) , Livesey (2000)
17	13-Jul-1982	28.84	2	0.01	Malta & Sardinia	-325 (0.0113%)	447		Livesey (1984)
18	17-Nov-1848	29.53	3	2.53	St Croix	n.a.	n.a.		Lang (1849) , Valach et al. (2019)
19	14-May-1921	30.21	3	0.02	east & west tips of Jamaica	[907±132]	831	New York Railroad Superstorm	Silverman & Cliver (2001) , Carapiperis (1956) Hapgood (2019) , Love et al. (2019a)
20	19-Aug-1950	30.84	1	0.68	Spetses, reece	-260 (0.0373%)	202	Photographic auroral report	Abbott & Chapman (1959)
21	25-Sep-1909	31.02	0	1.36	Niigata, Japan	[595]	576		Silverman (1995)

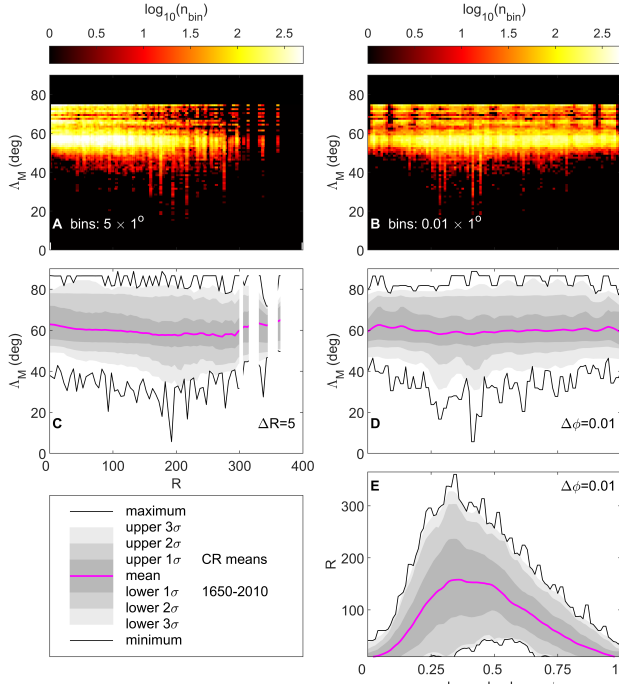


Figure 13. The variations of QD latitudes of the area-combined auroral samples, Δ_M , with sunspot number R and solar cycle phase ϕ (where $\phi = 0$ at the minimum in monthly R that marks the start of a cycle and $\phi = 1$ at the sunspot minimum that marks its end). Parts **A** and **B** are ‘data density plots’ (two-dimensional histograms). Part **A** shows the numbers of area-combined samples in bins that are 1° wide in Δ_M and 5 wide in R . **B** shows the numbers in bins that are again 1° wide in Δ_M and 0.01 wide in ϕ . Parts **C** and **D** show the same data as **A** and **B** in a different format: **C** corresponds to **A** and shows the variation of the Δ_M distribution with R and part **D** corresponds to **B** and shows the variation of the Δ_M distribution with ϕ . Part **E** shows the variation of the distribution of R as a function of ϕ . In parts **C**, **D** and **E**, the maximum and minimum of the Δ_M distribution are shown by black lines and the light grey, mid-grey and darker grey delineate values that are within, respectively, the $\pm 3\sigma$, $\pm 2\sigma$, and $\pm 1\sigma$ points of the distribution, the mean of which is shown by the mauve line.

In Section 3.6 we reduce the interval of interest to 1790–2024.5 (i.e., from just before the Dalton minimum to June 2024) for which only the yellow, orange and red contours of $\Delta_M = 31^\circ$ shown in Figure 12 apply. It can be seen that this removes the Middle-East/Arabia area as one where the threshold contour has moved. The first event in this interval that meets our criteria is in 1848 and so plots are for 1820 onward.

We also have studied how the distribution of area-combined observations has varied with sunspot number and the phase of the solar cycle, ϕ . We define ϕ to be zero at each sunspot minimum and to be unity at the subsequent minimum, and to vary linearly with time over the cycle in-between. The results are shown in Figure 13.

Panel **A** of Figure 13 shows a “data density plot” (a two-dimensional histogram) where the number of area-combined observations samples, n_{bin} is colour-coded for bins that are 1° wide in Δ_M and 5 wide in sunspot number R ; the colour coding being according to the scale given at the top. Panel **B** is the same for bins that are 1° wide in Δ_M and 0.01 wide in the solar cycle phase, ϕ . Panels **C** and **D** show the same data in a different format. The mauve lines are the mean values of Δ_M , as a function of R and ϕ , respectively (in bins of width $\Delta R = 1$ and $\Delta\phi = 0.01$) and the light grey, mid-grey and

darker grey bands delineate Δ_M values that are within, respectively, $\pm 3\sigma$, $\pm 2\sigma$, and $\pm 1\sigma$ points of the distribution, the means of which is shown my the mauve lines. The black lines are the maximum and minimum values of Δ_M in each bin.

Part **E** is in the same format as **C** and **D** but shows the variation of the distribution in R with ϕ , using bins of ϕ that are 0.01 wide. This plot shows the well-known behaviour that, on average, the solar cycle peaks at $\phi = 0.33$ but it peaks earlier if the sunspot number is higher than average, and later than this if R is lower than average.

Parts **A** and **C** of Figure 13 show that the aurora do shift to lower latitudes as R increases. At the highest latitudes the events become increasingly less frequent and are seen with only low frequency the largest R . Note, however, they are still seen. The mean of the distribution, and the lower 3σ , 2σ , and 1σ , points, all decrease with increasing R , up to about 250 where, rather surprisingly, they start to increase again. The lowest latitude reached is highly variable, reflecting the occurrence of a few extreme events. These events are most frequent and to lower latitudes at $200 < R < 250$ but they are less common and do not reach as low latitudes if R is larger than this range. This behaviour is in good agreement with the occurrence of extreme events of geomagnetic activity, as reported by Owens et al. (2021).

Parts **B** and **D** of Figure 13 show that all values, including the minima, are lower at sunspot maximum and that the largest excursions south almost always occur in the years around sunspot maximum. Again this agrees with the occurrence of extreme events of geomagnetic activity reported by Owens et al. (2021).

3.4 The greatest auroral events, in terms of the lowest geomagnetic latitudes reached

Between the Maunder and the Dalton minima, there are some scattered observations of aurora at latitudes below our threshold latitude of 31° . However, they are rare and isolated. For some of these nights the observation is the only one that was recorded, for others there are some others but these were all many degrees in magnetic latitude ($\Delta\Delta_M > 10^\circ$) poleward of the recorded low-latitude observation.

The first date for which we have records of auroral sightings from a range of latitudes is 17 November 1848. For this date, our database contains a total of 114 area-combined samples (at Δ_M between 29.53° and 72.7°), with aurora seen throughout Europe and the United States. The lowest magnetic latitude observation was from the tiny island of St Croix of the British Virgin Islands in the southern Caribbean Sea ($\Delta_G 17.72^\circ$ N, $\phi_G - 64.84^\circ$ E, at that date $\Delta_M = 29.53^\circ$), reported by Sir Andrew Lang, the governor of the island, who provided a highly plausible description of a low-latitude red aurora in Monthly Notices (Lang 1849). This was the only observations on that date that meet the $\Delta_M \leq 31^\circ$ criterion ($N = 1$). The nearest observation offers some confirmation and was from Havana in Cuba ($\Delta_G 23.13^\circ$ N, $\phi_G - 82.38^\circ$ E, at that date $\Delta_M = 32.06^\circ$) and so was just 2.53° poleward of the St Croix observation. The Havana observation was reported at the time in newspapers around the world, including the local ones in Cuba, and is listed in the catalogue of Fritz (1873). A range of latitudes reaching continuously down to the lowest point of observation is taken to show that St Croix, in this case, was not under a small isolated patch of mid-latitude aurora, which can occur — for example in localised SAR arcs. To limit this possibility, and to help expunge faked reports and misreported reports, we here require that the lowest two latitude stations are less than ten degrees apart in magnetic latitude ($\Delta\Delta_M < 10^\circ$) for a night to qualify as an extreme event, in addition to the minimum $\Delta_M \leq 31^\circ$ criterion (i.e. $N \geq 1$). This may well remove some genuine low-latitude auroral re-

sults from the early years, but such isolated reports cannot be relied upon.

Because there are no events that meet this criterion before the Dalton minimum and because of the large change in Λ_M contour location in the Middle-East and Arabia discussed in the last section, we here restrict the detailed study of events to after 1820. Events that reached down to, or below, this magnetic latitude in this interval are listed in Table 1, in which they are ordered by the lowest Λ_M reached. To gain to an event classification, we require at least one other area-combined sample be within 10° in Λ_M of the sample at $\Lambda_M \leq 31^\circ$. The 17 November 1848 event that reached down to St Croix is event number 18 in the list of 21 events.

Note that event number 21 (on 25 September 1909) is included in the list. This event just misses the threshold ($\Lambda_M = 31.142^\circ$) and the lowest magnetic latitude observation site, Niigata would have been above the threshold on other dates. We include it in Table 1 because it is so close to the threshold and within the uncertainty estimate. However, as there are a large number of events just above the threshold and we do not extend this exception to Figures 14 and 15.

Note also that we use the quoted date for an event and consider the second (astronomical) night of a long-lived storm as a separate event. This applies to the Carrington event and to the 10-11 May 2024 event. For many observations, we know this is valid because the same observer records the observations on both days and gives the universal or local time of the observations. However, some cases may be because the observer has moved the date forward by a day if the observation is made after local midnight; in which case the Day 2 observation is misplaced and should be in the Day 1 dataset. In the Carrington event, the Day 2 aurora reaches slightly lower latitudes than that reached on Day 1; however, for the May 2024 event, the Day 2 aurora does not reach as low a latitude as was seen on Day 1 by quite a wide margin.

Column 7 of Table 1 gives the minimum value of the geomagnetic D_{cx} index during the associated geomagnetic storm. For some events before 1932, we have estimates of the Dst index made by a variety of methods. One of these methods employ the low latitude extent of the aurora (Yokoyama et al. 1998), but as the reason for including minimum D_{cx} values and Dst estimates in Table 1 is to compare with the minimum Λ_M values, this is not appropriate. In addition, Hayakawa et al. (2023b) note that the method almost certainly gives Dst values that are unrealistically too large when extrapolation is extended to the very largest of auroral events. The values in square brackets are estimates of the storm's minimum Dst value: the letters "n.a." in square brackets are used if no such estimate is available. There have been a number of estimates of the minimum Dst value during the storm associated with the extreme auroral events of August/September 1859 and these vary between -800nT and about -1600nT. It is important to estimate hourly values (Siscoe et al. 2006) to compare with D_{cx} values. The value quoted for these events in Table 1 is that derived by Love et al. (2024) and agrees quite well with an independent estimate by Cliver & Dietrich (2013). The value for the 14 May 1921 event is from Love et al. (2019b) and for the 25 September 1909 event (that does not quite meet our $\Lambda_M \leq 31^\circ$ criterion) is from Hayakawa et al. (2019).

For many events, for example, that of 14 May 1921 (19 in the ranked order) the lowest latitude observation of aurora was made by known individuals and is well corroborated. In this case it was made by the staff of the Morant Point Lighthouse at the east tip of the island of Jamaica ($\Lambda_G 17.92^\circ$ N, $\phi_G -76.18^\circ$ E, at that date $\Lambda_M 30.36^\circ$) and recorded by the lighthouse superintendent, Mr. C. Durrant. It was also seen by the staff of the Negril Point lighthouse at the west end

of the island, which is at a magnetic latitude that is only marginally greater ($\Lambda_G 18.25^\circ$ N, $\phi_G -78.36^\circ$ E, at that date $\Lambda_M 30.27^\circ$). It was also recorded by the superintendent there, a Mr. J.S. Brownhill. The aurora was also seen in Graham Town just north-east of Kingston and midway between the two lighthouses and recorded in considerable detail by Lieutenant A.W. Tucker, who describes what we now recognize to be a diffuse red glow mixed with some rays of an green-line arc. In all three cases, the aurora was reported as being to the north. This was all recorded by Herbert Lyman in his survey of the event, published two months after the event in Monthly Weather Review (Lyman 1921). As well as there being three corroborating observations, there is an almost continuous distribution of sightings at greater Λ_M from observers on a trading ship south of Cuba, in Mexico, all throughout the USA, and in Southern Canada, France, England, Scotland, and Scandinavia. Hence, the auroral expansion down to the minimum latitude is well-defined in this case. However, we note there is an isolated report closer to the equator, from Apia in Samoa in the Southern Hemisphere. However, this observation was in daylight and studying the newspapers from Honolulu reveals no mention of aurora, which would be expected as it is as a similar Λ_M (but in the northern rather than the southern magnetic hemisphere). Hence in this case the minimum Λ_M , in the Northern Hemisphere at least, is very well-defined.

The event on 14 July 2000, referred to as "Bastille Day" storm, demonstrates a cautionary point about our event definition. At the peak of that storm, an image taken by the Polar spacecraft UV imager showed aurora between magnetic latitudes of 26.24° and 67.32° over eastern America and the Caribbean. However, cloud cover was remarkably omnipresent in this area during the event and reports of observations are rare: our dataset contains just 19 area-combined samples on this day. This was also at the time that newspaper reporting of aurora was in decline and social media reporting was in its infancy. Nevertheless, the ground based observations do (just) meet our criteria. The lowest latitude observation was from Mexico City; however, this is only known because newspapers picked up the story of people collecting in Chapultepec Park in the city ($\Lambda_G 19.42^\circ$ N, $\phi_G -99.19^\circ$ E, at that date $\Lambda_M 28.43^\circ$) to view what they thought was an alien invasion! This was later confirmed to be aurora by a nearby astronomical observatory. The next lowest magnetic latitude auroral report on that night was from Split, Croatia ($\Lambda_G 43.52^\circ$ N, $\phi_G 16.5^\circ$ E, at that date $\Lambda_M 37.94^\circ$), communicated to the British Astronomical Association by British tourists in the region (Livesey 2000). Hence, this event has a $\Delta\Lambda_M$ value of 9.51° and is just under our threshold criterion. The point is that, despite the potential for observations over much of the Northern Hemisphere, it is possible that our survey has missed an event at a time when reporting was low, and/or cloud cover was extensive at the longitude of midnight magnetic local time at the time of peak disturbance.

The 25 September 1909 event raises another important point about our survey. Silverman (1995) discounts a reported sighting on this night from Singapore ($\Lambda_G 1.34^\circ$ N, $\phi_G 103.83^\circ$ E). If valid, this report would give $\Lambda_M -7.69^\circ$ and be, arguably, the closest ever aurora to the magnetic equator. However, this does not meet our $|\delta\Lambda_M| < 10^\circ$ criterion, being more than 24° closer to the magnetic equator than the Niigata sighting. Silverman (1995) notes that this report originates only from a newspaper article and likely refers to a disruption of cable transmissions. Likewise, Silverman discounts a newspaper report from Shimla (formerly Simla), India on this day ($\Lambda_G = 31.15^\circ$ N, $\phi_G = 77.25^\circ$ E, $\Lambda_M = 24.12^\circ$). This is because George C. Simpson (later Sir George and President of the Royal Meteorological Society) was working at the Indian Meteorological Service headquarters in Shimla at the time. He had a particular

interest in geomagnetic and auroral events and always included them in national Meteorological reports. However, on this date he mentions no aurora, not only in Shimla but anywhere in India or Central Asia in general. In a letter to Nature, however, he does mention a geomagnetic disturbance at Shimla during this night and it is likely that this too, at some stage, was wrongly interpreted as also revealing aurora. This report would be allowed by our criteria. In the Southern Hemisphere, the September 1909 event was seen widely in Australia but not in Indonesia, which you would expect were Singapore or Shimla really correct. That leaves the lowest confirmed geomagnetic latitude on this night as Niigata in Japan ($\Lambda_G = 37.9^\circ$ N, $\phi_G = 139.1^\circ$ E, at that date $\Lambda_M = 31.12^\circ$). If the Shimla report were valid (and not another report of cable disruption, which is the most likely explanation) this would raise event 21 to 11 in the ranked order. This change is not important in itself but does remind us that single reports can alter the ranking order considerably.

3.5 The lowest magnetic latitude of auroral observations

The question of the lowest geomagnetic latitude from which aurora can be seen needs to be addressed. Figure 4 shows that the QD and dip equators are almost identical, so the magnetic field is horizontal at the geomagnetic equator. For the field line to reach up into the magnetosphere, we have to move to non-zero $|\Lambda_M|$. We can get an estimate using invariant magnetic latitude, Λ_I which is defined from $L = 1/(\cos(\Lambda_I))^2$, where for a dipole field, L is the geocentric height of the equatorial apex of the field line in units of Earth radii ($R_E = 6370\text{ km}$). For $\Lambda_I = 10^\circ$, this gives a maximum (apex) field line altitude h of just 198 km, which is below the ionosphere: $\Lambda = 20^\circ$ gives $h = 834\text{ km}$ ($0.33R_E$), $\Lambda = 30^\circ$ gives $h = 2123\text{ km}$ ($1.4R_E$), $\Lambda = 40^\circ$ gives $h = 4485\text{ km}$ ($0.7R_E$) and $\Lambda = 50^\circ$ gives $h = 9047\text{ km}$ ($1.4R_E$). Shiokawa et al. (2013) used ground-based and satellite observations to estimate that mid-latitude, storm-time, red aurora originated from magnetospheric populations of at L of about 2 which corresponds to $\Lambda_I \approx 45^\circ$. Hence, it is very difficult to conceive of auroral precipitation at Λ_I below about 30° (Silverman & Cliver 2001).

However, these considerations relate to the magnetic latitude of coronal auroral forms, where the observer is close to being on the field line down which the causal particles precipitate. The lowest-latitude auroras in our dataset are not coronal forms, they are viewed at low elevation angles (β) from locations equatorward of the field lines on which the precipitation is occurring. To investigate how far to the south is possible, we use the dipole field geometry shown in Figure 9 of Hayakawa et al. (2023b). The altitude of the emission, h influences this calculation because higher altitude aurora can be seen from further away. The emission altitude of mid-latitude storm-time red aurora has been studied by Kataoka et al. (2024) and they found it was detectable up to h of about 600 km. This was estimated using sophisticated and scientific instruments with sensitivity greater than that of the human eye and so we here use $h = 600\text{ km}$ as a maximum altitude from which a human observer could detect such an aurora. The formula needed to compute the latitude of observation Λ_M for an observing elevation angle β and emission at an altitude h on a field line that reaches Earth's surface at QD latitude of Λ_F is

$$\Lambda_M = \left\{ \cos^{-1} \left(a^{1/2} \cdot \cos \Lambda_F \right) \right\} + \left\{ \frac{\pi}{2} - \beta - \sin^{-1} \left(\frac{\cos \beta}{a} \right) \right\} \quad (4)$$

where $a = (R_E + h)/R_E$ and R_E is the radius of Earth's surface. The first term in 4 accounts for the difference in latitude between the point of emission and the latitude where the field line reaches

Table 2. Values of QD latitude Λ_M from which an aurora could be observed at elevation β for emission along an auroral field line of QD latitude Λ_F at an altitude h .

Λ_F (°)	30	30	30	40	40	40	50	50	50
h (km)	200	400	600	200	400	600	200	400	600
β									
0°	14	7	1	25	18	13	35	29	24
5°	18	11	6	29	23	17	39	33	28
10°	21	15	9	32	26	21	42	36	32
15°	22	17	12	33	28	24	44	39	35
20°	24	19	14	34	30	26	45	41	37

the ground (Λ_F) and the second term accounts for the difference in latitude between the point of emission and the observer at Λ_M .

Table 2 gives values of the QD latitude of a ground-based observer Λ_M who is able to see aurora at an elevation β above the horizon for auroral precipitation down field lines of QD latitudes Λ_F of 30°, 40° and 50° and emission altitudes of h of 200 km, 400 km and 600 km. These values all assume a dipole field model. The top row is the limit (zero elevation) but aurora would not be detectable and a higher β is required. The table shows that Λ_M is only below 10° for exceptionally high h and exceptionally low Λ_F . We therefore conclude that the likelihood of detecting aurora from $\Lambda_M < 10^\circ$ is very low indeed and reports from such sites are not plausible and should be treated with great suspicion.

This issue is raised by what is generally agreed to be the most extensive auroral event known — that of 4 February 1872. This event is often called the *Secchi Event* as it was observed and recorded in some detail by Angelo Secchi in Rome (Berrilli & Giovannelli 2022). Notably, Secchi used simultaneous observations by a wide variety of different instruments — he even noted some effects on global technological systems, in particular telegraph networks. The lowest magnetic latitude of a sighting on that night is a matter of some debate. In our database there are 9 independent and credible reports of aurora on 4 February 1872 from Mumbai (Bombay) in India ($\Lambda_G = 19.12^\circ$ N, $\phi_G = 72.87^\circ$ E, on that date $\Lambda_M = 9.71^\circ$) and several reports from elsewhere in India and Pakistan

Table 3 lists all 52 sites at which aurora was reported on 4 February 1872 that are at $\Lambda_M \leq 31^\circ$. Note there are 3 sites where there may have been auroral sightings at even lower magnetic latitudes than Mumbai, these are Gondokoro in Sudan, Aden in Yemen and Khartoum in Sudan. The table shows that there are considerable numbers of sightings at the longitudes of the Middle East and Arabia, at somewhat higher (but still low) latitudes. However, the lowest three Λ_M values are so low, the discussion given above means that we need to treat them with a considerable degree of scepticism. They, in fact, originate from just one source. Opinions differ, Hayakawa et al. (2023b) argue they are valid, whereas Silverman (2008) argues that they are almost certainly misinterpretations of cable disruption reports. The magnetic latitudes used by Hayakawa et al. (2023b) are computed using the procedure established by Vestine based on the pole locations of a fitted geocentric dipole and are the estimated precipitation latitudes Λ and not the observation Λ_M values used here. Using the more accurate gufl model (for this date) we get magnetic latitudes that are less plausible for these three sites. As a result, we tend to agree with Silverman and have omitted these three reports (they are listed in Table 3 but not numbered in the ranked list).

Table 3 shows that although the extremely-low latitude sightings during the Secchi event were mainly in the Indian/Pakistan subcontinent and in the Middle-East/Arabia sectors, there is a global range

Table 3. Locations from where aurora was observed with QD latitude Λ_M below the 31° threshold from where aurora was observed on 4 February 1872 ranked by increasing Λ_M value. The geographic coordinates of the sites are (Λ_G, ϕ_G).

#	Λ_G (° N)	ϕ_G (° E)	Λ_M (° N)	location name
—	4.90	31.67	-5.58	Gondokoro, Sudan
—	12.81	45.03	2.34	Aden, Yemen
—	15.58	32.53	5.85	Khartoum, Sudan
1	19.12	72.87	9.71	Mumbai, India (Bombay)
2	18.86	82.57	10.11	Jeyapore, India
3	21.39	39.86	11.86	Al-Moabdah, Makkah (Mecca)
4	21.76	72.15	12.52	Bhavnagar, India
5	24.09	32.9	15.25	Aswan, Egypt (Syene)
6	25.65	57.79	16.28	Bandar-e-Jask, Iran
7	25.45	81.85	17.07	Allahabad, India
8	26.86	80.94	18.52	Lucknow, India
9	27.72	68.82	18.78	Sukkur, Pakistan (Aror or Bakhar)
10	27.04	88.26	19.26	Darjeeling, India
11	28.28	68.44	19.37	Jacobabad, Pakistan
12	30.17	71.47	21.53	Multan, Pakistan
13	29.97	32.55	21.84	Suez, Egypt
14	30.05	31.24	22.05	Cairo, Egypt
15	31.22	29.95	23.48	Alexandria, Egypt
16	32.69	51.69	23.95	Ispahan, Iran
17	32.37	75.60	24.08	Madhopore, India
18	30.00	120.58	24.08	Shaoxing, Zhejiang, China
19	11.22	-60.78	24.09	Courland Bay, Tobago
20	32.94	73.72	24.61	Jhelum, Pakistan
21	32.68	35.60	24.62	Masada, Israel (Sebbeh)
22	33.56	73.04	25.24	Rawalpindi, Pakistan
23	31.23	121.49	25.30	Shanghai, China
24	32.19	111.55	26.14	Shengkangzhen, Hebei, China
25	32.38	111.68	26.36	Laohekou,Xiangyang,Hubei,China
26	35.49	74.59	27.38	Raikot, Pakistan (Raikote)
27	33.63	130.23	27.54	Kota, Fukuoka, Japan
28	33.97	135.12	27.74	Yura, Wakayama, Japan
29	33.87	130.65	27.76	Onga, Fukuoka, Japan
30	34.27	133.03	28.09	Imabari, Ehime, Japan
31	34.27	108.95	28.16	Xincheng,XiAn,Shaanxi,China
32	22.16	-100.97	28.35	San Luis Potosí, Mexico
33	34.72	137.73	28.42	Hamamatsu, Shizuoka, Japan
34	34.67	131.85	28.51	Masuda, Shimane, Japan
35	34.83	136.87	28.55	Tokoname, Aichi, Japan
36	34.90	132.10	28.73	Hamada, Japan
37	35.00	135.75	28.74	Kyoto, Japan
38	34.75	113.68	28.78	Zhengzhou, Henan, China
39	35.18	136.90	28.89	Nagoya, Japan
40	35.15	132.40	28.97	Oda, Shimane, Japan
41	35.37	132.75	29.18	Izumo, Shimane, Japan
41	35.68	139.75	29.32	Chiyoda City, Tokyo, Japan
42	35.53	129.33	29.43	Ulsan, South Korea
43	35.95	139.7	29.59	Saitama, Japan
44	18.47	-69.95	29.83	Santo Domingo, Dominican R.
45	36.32	139.80	29.94	Oyama, Japan
46	36.37	140.47	29.98	Mito, Ibaraki, Japan
47	36.38	139.73	30.01	Tochigi, Japan
48	36.25	111.68	30.24	Linfen, Shanxi, China
49	36.65	128.45	30.56	Yecheon-gun, South Korea
50	37.03	140.38	30.64	Tanagura, Fukushima, Japan
51	37.05	140.88	30.65	Iwaki, Fukushima, Japan
52	35.84	14.54	30.96	Marsaxlokk, Malta

Table 4. Locations from where aurora was observed with QD latitude Λ_M below the 31° threshold on 10 and 11 May 2024, ranked by increasing Λ_M value. The geographic coordinates of the sites are (Λ_G, ϕ_G).

#	Λ_G (° N)	ϕ_G (° E)	Λ_M (° N)	location name
1	22.92	57.53	18.08	Ad Dakhiliyah, Oman
2	23.32	57.13	18.51	Jabal al Sarat, Oman
3	28.27	-16.64	19.12	El Teide, Tenerife
4	27.96	-15.57	18.46	Pico de las Nieves, Gran Canaria
5	27.88	-15.72	18.58	Mogán, Las Palmas, Gran Canaria
6	27.99	-15.57	18.70	Cueva Grande, Gran Canaria
7	19.07	-155.58	19.49	Nā'Ālehu, Big Island, Hawaii
8	19.07	-155.58	19.49	Breña Alta, Santa Cruz de La Palma
9	28.76	-17.88	19.83	Roque de Los Muchachos Observatory, La Palma
10	28.78	-17.96	19.86	Astronorte Observatory, La Palma
11	20.92	-156.38	21.09	Kuau beach, Maui, Hawaii
12	14.72	-90.65	24.65	San Juan Sacatepéquez, Guatemala
13	18.41	-66.22	24.85	Candelabra, Puerto Rico
14	18.09	-67.12	24.89	Monte Grande, Puerto Rico
15	19.09	-96.14	28.33	Heroica Veracruz, Mexico
16	35.30	139.44	28.37	Hiratsuka, Kanagawa, Japan
17	19.30	-81.38	29.25	Georgetown, Cayman Islands
18	36.10	138.49	29.26	Koumi, Nagano, Japan
19	34.14	77.56	29.81	Ley, India
20	34.01	58.17	29.98	Ferdows, South Khorasan, Iran
21	34.01	58.17	29.98	İstanbul, Türkiye
22	37.03	14.70	30.36	Chiaramonte Gulfi, Ragusa, Sicily
23	20.73	-89.00	30.68	Yucatán, Mexico (10 May)
24	20.73	-89.00	30.68	Yucatán, Mexico (11 May)
25	37.38	136.91	30.70	Wajima, Ishikawa, Japan
26	37.65	140.02	30.79	Kitakata, Fukushima, Japan
27	22.65	-100.61	30.92	Peyote, San Luis Potosí, Mexico
28	38.37	-7.51	31.00	Alqueva, Portugal

of longitudes ϕ_G between -101.0° (San Luis Potosí, Mexico) and 104.5° (Mito, Japan).

Note that the furthest poleward sighting during the Secchi event was at Polaris Bay, Greenland from the expedition ship “Polaris” ($\Lambda_G 81.36^\circ$ N, $\phi_G 62.15^\circ$ E, at that date $\Lambda_M 73.44^\circ$). Interestingly, the aurora even at that high latitude was described as a brilliant red, which was the dominant description all over the globe (Silverman 2008).

Table 4 is the same as Table 3 for the May 2024 event. In this case, observations on both 10 and 11 May 2024. Comparison shows that not only does the May 2024 event not reach as low latitudes as the Secchi event, but also the number of observations below the threshold magnetic latitude is very much lower. There is one, unconfirmed, report on May 11 from Dawwah on Masirah Island off the south-east coast of Oman at $\Lambda_M = 15.51^\circ$ which, if confirmed, would lift the 11 May event to second in the ranked list in Table 1. However, no details nor image are available to help confirm the report. On the other hand, the two reports to the west of Muscat have been confirmed and the one at Jabal al Sarat, in the Al Hajar al Gharbi Starlight Reserve, was made by the Oman Astronomical Society and NASA have confirmed it as an auroral sighting.

3.6 Events that meet the 31-degree threshold

Figure 14A plots all the area-combined samples on the dates of events 1–20 in Table 1. These are plotted as a function of date on top of horizontal bars of different shades of grey and a mauve line that give the distribution and mean of Λ_M for all samples in the database,

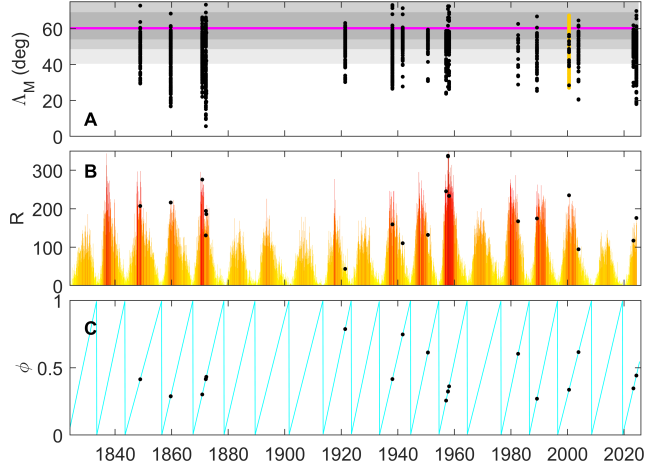


Figure 14. Analysis of extreme auroral events in which aurora extends to geomagnetic latitudes below the $\Lambda_M = 31^\circ$ threshold defined in Figure 11, for January 1820 to June 2024. **A** the black points show the Λ_M of area-combined samples on days classed as extreme events. The bars of different shades of grey and the mauve line give the distribution and mean of Λ_M for all samples in the database, using the same format as in Figure 13. The orange bar for the "Bastille Day" event of 14 July 2000 gives the range of Λ_M derived from global auroral images from UV imager on the Polar spacecraft which is used because cloud cover and the timing of the event combined to give fewer ground-based observations of aurora in this event at the lowest Λ_M . **B** Carrington Rotation means of sunspot number, R , in the same format as Figure 8B. The black points are the values for the CR containing the extreme event. **C** The solar cycle phase variation, ϕ , with the black points marking the extreme events.

using the same format as in Figure 2A. The orange bar shows the maximum extent of the midnight auroral oval seen by the UV imager on the Polar satellite during the Bastille-day storm, and the lack of black points emphasizes the paucity of ground-based observations for this event. Panel B gives the Carrington Rotation means of the sunspot number, R , using the same coloured bar-chart format as Part B of Figure 8. Panel C shows the solar cycle phase, ϕ . In parts B and C the black dots mark the date of the events. The plot confirms that events are generally near the peak of the sunspot cycle, although the 1921 and 1941 events are more in the middle of the declining phase. The 1921 event was at considerably lower sunspot number than any other event. The plot shows that neither large sunspot numbers nor cycle maximum guarantee an event.

The top panel of Figure 15 is the same as that in 14 and panel C compares it to Carrington Rotation means of the mid-latitude aa_H geomagnetic index. This shows that the events defined in Table 1 are always accompanied by a geomagnetic storm of some magnitude. However, some very large geomagnetic storms are not accompanied by a large global auroral event. The relationship of the auroral events to the geomagnetic storms will be the subject of a later paper.

Lastly, Panel B of Figure 15 shows Carrington Rotation means of the signed open solar flux, F_S , as generated by Lockwood & Owens (2024). These are estimated using four geomagnetic activity indices (including aa_H) and calibrating the algorithm using the modern satellite F_S estimates by Frost et al. (2022) who used strahl electrons and the method developed by Owens et al. (2017b) to allow for the "excess flux" caused by inversions of the open field lines in the heliosphere (now often called "switchbacks") (Lockwood et al. 2009a,b). Comparing with Figure 14B, it is noticeable that high

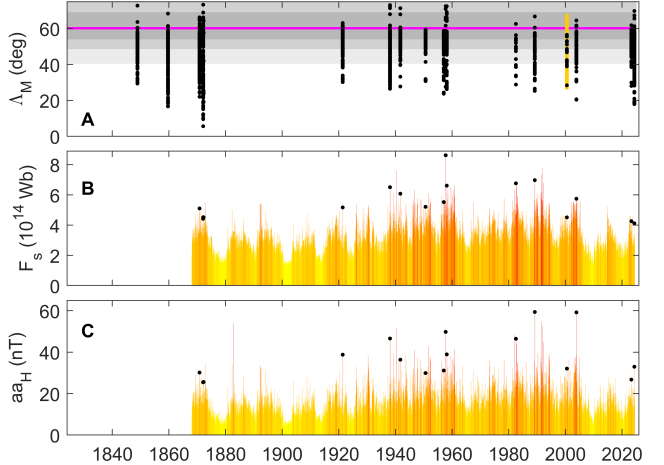


Figure 15. **A.** The same as Figure 14A. **B** the same as 14B for CR means the homogeneous aa index, aa_H , (Lockwood et al. 2018a,b). **C**, the same as part B for the signed open solar flux F_S (Lockwood & Owens 2024). The events all occur during Carrington Rotations when F_S exceeds 4×10^{14} Wb, but there are a great many Carrington Rotations when F_S exceeds this value but no extreme event occurs at Earth.

open solar flux is a more important criterion for an extreme auroral event than high sunspot number. In the interval for which we have Carrington Rotation (CR) means of F_S (1868–2024.5) all 17 CRs in which an extreme auroral event occurred had a mean F_S that exceeded 4×10^{14} Wb; however, there were 476 CRs in which this threshold was exceeded but no extreme event is seen, so only 3.6% of CRs exceeding this F_S threshold gave an auroral event. Hence, exceeding this threshold in open solar flux is a necessary, but far from sufficient, condition.

3.7 Relationship to solar Active Regions

Figure 14B shows that, although none of these extreme auroral events occur at sunspot minimum, they do not require an especially high sunspot number. This point is emphasized by the "Halloween" events of October/November 2003 that was followed by the 20 November 2003 extreme auroral event. This interval is shown in Figure 16, in the same format as Figure 2. Note that comparison of Panel A of Figures 2 and 16 reflects how much internet reporting of auroras grew between 2003 and 2015.

The series of events referred to as the "Halloween Storms" began on October 29 and on three successive nights aurora was seen at unusually low latitudes. However, the lowest magnetic latitude reached was only $\Lambda_M = 34.34^\circ$ and so these nights do not meet the $\Lambda_M = 31^\circ$ threshold that we have set to define extreme events. Figure 16 shows that just 22 days after the onset of the first Halloween storm (i.e., significantly less than a full Carrington rotation period), there was another event on 20 November that does meet our threshold and in which the geomagnetic disturbance in both the aa_H and the D_{cx} indices (panels B and C, respectively) was larger than seen in the events of 29–31 October. This is despite the fact that the sunspot number, shown in panel D, was considerably lower than it had been during the Halloween storms.

Table 5. Areas of sunspot groups identified as the origin of CMEs that generated the 21 extreme auroral events listed in Table 1 compared with the effects of the 21 largest sunspot groups by area (note that the 13 March 1989 and the Fátima storm of 25 January 1938 fall into both these categories), plus the St Patrick’s Day storm studied in Figure 2. For the 21 large-area spot group cases, the peak disturbance (minimum Δ_M , maximum aa_H and minimum D_{cx}) is taken for interval between the large group first appearing and one day after (to account for propagation time to Earth) it has rotated off the disc. Note also that group 12673, which peaked in area at $3267\mu sh$ on 21 January 1938, generated two geomagnetic/auroral storms. The second of these was the larger and is the Fátima Storm, ranked number 13 in the list of exceptional storms listed in Table 1: this was caused by a CME launched just before the group rotated off the east limb of the Sun. The areas given are the maximum whole spot group area (in millionths of a solar hemisphere) attained by the group in question. The rank number (available down to #24) is by the peak area of the sunspot group (Meadows 2024). References giving the group area are: a.Meadows (2024); b.Hayakawa et al. (2021); c.Debrecen Photoheliographic Database; d.Hayakawa et al. (2024); e.Love & Coïsson (2016); f.Ishkov (2016) (English translation available from ResearchGate); g. Love et al. (2019a); h.Hayakawa et al. (2023b); i.Silverman (1995).

1 Event Date	2 Group number	3 Group area (μsh)	4 area rank	5 ref	6 minimum Δ_M ($^\circ$)	7 $P_{LT}(\Delta_M)$ (%)	8 minimum D_{cx} (nT)	9 $P_{LT}(D_{cx})$ (%)	10 maximum aa_H (nT)	11 $P_{GT}(aa_H)$ (%)
8-Apr-1947	14886	6132	1	a,c	46.7	0.7732	-78	1.5816	96	1.0371
7-Feb-1946	14417	5202	2	a,c	39.1	0.1216	214	0.0755	99	0.0191
19-May-1951	16763	4865	3	a,c	52.0	3.8742	-47	5.4040	41	9.2713
29-Jul-1946	14585	4720	4	a,c	42.1	0.2934	-246	0.0463	322	0.0356
12-Mar-1947	14851	4554	5	a,c	40.1	0.1471	-195	0.0997	186	0.1600
24-Oct-2014	12192	4419	6	a,c	50.0	1.9919	-50	4.6968	78	1.8719
13-Mar-1989	5395	4201	7	a,c	25.3	0.0095	-564	0	722	0.0007
16-Nov-1990	6368	3827	8	a,c	50.6	2.5039	-143	0.2818	170	0.2006
19-Jan-1926	9861	3716	9	a,c	33.1	0.0588	n.a.	-	343	0.0298
21-Jan-1938	12673	3627	10	a,b,c	31.9	0.0407	-326	0.0110	650	0.0017
				and	26.5	0.0104	-336	0.0090	656	0.0015
14-Feb-1917	7977	3590	11	a,c	48.8	1.3024	n.a.	-	141	0.3399
30-Oct-2003	10486	3338	12	a,c	34.3	0.0683	-372	0.0044	698	0.0011
29-Mar-2001	9393	3387	13	a,c	38.1	0.1021	-380	0.0036	298	0.0432
20-Jul-1938	12902	3379	14	a,c	57.0	17.355	-125	0.4346	125	0.4734
5-Oct-1937	12553	3340	15	a,c	38.7	0.1106	-171	0.1554	126	0.4626
2-Feb-1905	5441	3339	16	a,c	40.1	1.4081	n.a.	-	155	0.2676
28-Jul-1937	12455	3303	17	a,c	48.8	1.3024	-165	0.1748	221	0.1024
26-Apr-1937	4474	3274	18	a,c	53.6	6.5206	-91	1.0577	159	0.2462
23-Mar-1991	6555	3257	19	a,c	41.9	0.2461	-281	0.0249	362	0.0249
16-Jun-1989	5528	3249	20	a,c	45.0	0.5217	-132	0.3675	105	0.7748
27-Oct-1991	6850	3234	21	a,c	38.9	0.1166	-280	0.0256	267	0.0596
1-Sep-1859	C520	3100	24	a,c	18.6	0.0044	n.a.	-	n.a.	-
13-Jul-1982	3804	3092	-	c	28.8	0.0160	-325	0.0113	447	0.0126
10-May-2024	13664	2761	-	d	18.1	0.0023	-390	0.0031	521	0.0070
18-Sep-1941	13937	2598	-	e,c	27.7	0.0130	-404	0.0026	459	0.0112
28-Aug-1859	C520	2300	-	f	16.7	0.0015	n.a.	-	n.a.	-
14-May-1921	9334	1709	-	g	30.2	0.0175	n.a.	-	831	0
14-Jul-2000	9077	1591	-	c	28.2	0.0142	-295	0.0197	352	0.0247
15-Mar-2015	12297	788	-	c	36.6	0.0848	-215	0.0740	264	0.0622
4-Feb-1872	S29	627	-	h	9.7	0	n.a.	-	626	0.0022
19-Aug-1950	16588	574	-	c	30.8	0.0222	-260	0.0373	202	0.1320
21-Jan-1957	17829	557	-	c	23.7	0.0073	-255	0.0400	416	0.0169
20-Nov-2003	10501	510	-	c	20.4	0.0058	-418	0.0021	564	0.0050
25-Sep-1909	6728	362	-	i,c	31.0	0.0233	n.a.	-	576	0.0039

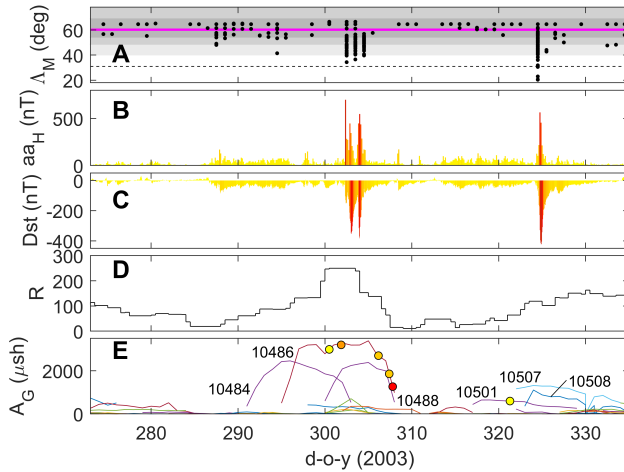


Figure 16. Analysis of the “Halloween” events of October/November 2003, followed by the 20 November 2003 extreme auroral event. The format is the same as Figure 2. In part E the numbers are the numbers of the sunspot groups labelled in Figure 17 and yellow dots denote the occurrence of an M-class flare in that sunspot group and orange and red points denote X-class flares, the red point being the largest flare ever recorded. The horizontal dashed line in A is the 31° threshold of Λ_M used in this paper to define extreme auroral events.

Panel E shows that there was a rapid rise in group area, particularly group 10486, before the October 29–31 (Halloween) events, but the groups were of much more modest area before the 20 November event. Hence, these events demonstrate that neither sunspot number nor the size of sunspot groups is a good predictor of the size of subsequent auroral and geomagnetic disturbances. In fact, the CME and associated flare that gave rise to the 20 November 2003 storm was in group 10501 (Srivastava et al. 2009), which was not even the largest group on the disc at the time and was very small compared to the group 10486 which produced multiple X-class flares.

Parts C and F of Figure 17 compare the solar disc the days before, respectively, the first Halloween storm and the 20 November storm. The Halloween storms were largely associated with an X17 flare in region 10486 on 28 October, when the group was close to the central meridian as shown in part C: this group was responsible for a series of flares and subsequently generated an X2, an X3 and a massive X28e (estimated) flare when close to the western limb, shortly before rotating off the visible disc. On the other hand, part F shows the much smaller group at the centre of the disc that was responsible for the 20 November storm. The inserts show detailed views of the two groups. The key point is that the group causing the Halloween storms was much larger in area and generated more and larger flares, but the 20 November storm was larger in both auroral area and geomagnetic disturbance. This case illustrates that sunspot group area is not a good predictor of the storm amplitude. This raises two possibilities. Firstly, it may be that big sunspot groups can untangle complex field structures with many small releases of energy and material and hence without the release of a large CME. Alternatively, the internal structure in a CMEs released by a big sunspot group may be more complex. The latter possibility could have two effects: firstly the geoeffectiveness of a CME could depend on which part of it impacts Earth’s magnetosphere (c.f. Owens et al. 2017a); secondly the field at Earth might vary more and so there is no prolonged interval of strongly southward Interplanetary Magnetic Field that gives sustained transfer of solar wind energy into the magnetosphere.

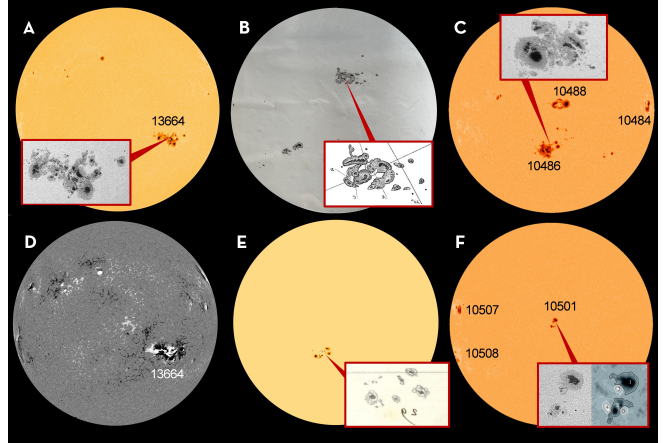


Figure 17. Active region sunspot groups associated with events ranked 1, 3, 4, 5, and 6 in Table 1. Sunspots groups are labelled with the AR numbers assigned by NOAA. A. Continuum image of the Solar disc made by the HMI (Helioseismic and Magnetic Imager) instrument on SDO (Solar Dynamics Observatory) on 10 May 2024 showing sunspot group 13664 (shown in greater detail in the inset): Part D beneath A shows the magnetogram taken simultaneously by the same instrument. B Richard Carrington’s sunspot group drawing for 1 September 1959 (reproduced courtesy the Royal Astronomical Society of London). E beneath B shows a reconstruction of the sunspot group near the centre of the solar disc that is thought to have given rise to the storm of 4 February 1872: this is drawn from the common elements of the solar drawings for 3 February by Angelo Secchi and Louis Beraerts: the inset shows the sketch by Secchi (from Hayakawa et al. 2023b). C Continuum image of the Solar disc made by the MDI (Michelson Doppler Imager) instrument on SoHO (Solar and Heliospheric Observatory) satellite on 29 October 2003 showing sunspot group 10484 (shown in greater detail in the inset): Part F beneath C shows the solar disc 22 days later seen by the same instrument on 20 November 2003 with just one central group (10501): the inset shows the active region and a magnetogram plot, revealing the magnetic structure (Oreshina et al. 2012).

Because the 10 May 2024 event was associated with an exceptionally large sunspot group (see parts A and D of Figure 17) as, famously, was the Carrington event (see part B), there is a widespread belief that these events are always generated by exceptionally large sunspot groups and that exceptionally large sunspot groups always drive great auroral events. Neither of these two assumptions is correct. The point is illustrated by Figure 17E which is a reconstruction of the group that generated the greatest known auroral event, that of 4 February 1872, which was not at all exceptional in area.

Table 5 and Figure 18 demonstrate the lack of a consistent relationship between source sunspot group area and the extent of the auroral event. Columns 7, 9 and 11 show where a given value sits in the overall distribution of that particular parameter. The auroral dataset for 1650–2024.5 covers 136966 nights. For nights with no auroral observation, the minimum value of Λ_M is taken to be greater than 70° , on the grounds that auroral always exists at some latitude, even if it is a very high latitude. Column 7 gives the percentage, $P_{LT}(\Lambda_M)$, of the 136966 nightly minima of Λ_M that are smaller than the value given in Column 2. Between 1932 and 2015 there are 739968 definitive hourly values of D_{cx} that range between $+108nT$ and $-565nT$ and this gives us a reference distribution of D_{cx} values to help evaluate the relative magnitudes of the various storms in the ring current: column 8 gives the percentage of the 739968 D_{cx} values that are more negative than the minimum value for that storm, $P_{LT}(D_{cx})$. Between 1868 and 2024.5 there are 457240 3-hourly values of aa_H

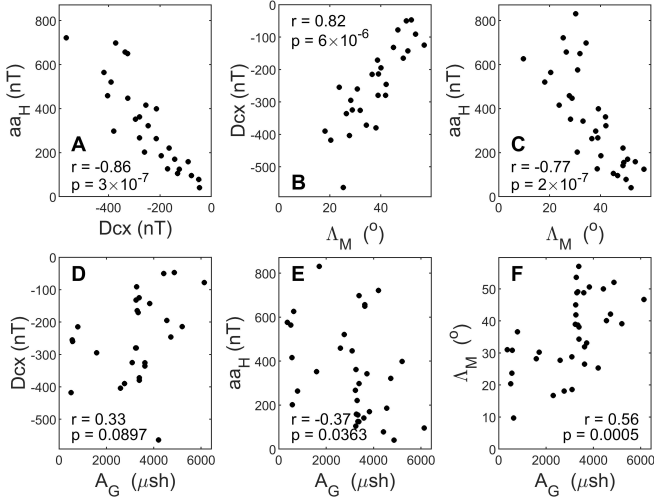


Figure 18. Scatter plots of the relationships between the peak geomagnetic disturbances in indices Dcx and aa_H , the area of the causal sunspot group, A_G and the lowest latitude QD magnetic latitude at which the aurora was seen, Λ_M . In each case, the correlation coefficient r is given with the p -value of the null hypothesis that there is no correlation or anticorrelation: values of p below 0.05 indicate a correlation that is significant at the 2σ level. The dataset is the list of events given in Table 5.

that range between 0.37 nT and 831.52 nT: column 11 of Table 5 gives the percentage of these values that are greater than the corresponding aa_H value in column 10, $P_{GT}(aa_H)$. These percentages quantify how extreme an event was, as quantified by the parameter in question. Note that $P_{LT}(\Lambda_M) = 0$ for the 4 February 1872 (Secchi) event because that is the most equatorward aurora in the record. Similarly, $P_{LT}(Dcx) = 0$ for the 13 March 1989 event as the lowest recorded Dcx value was during this storm and $P_{GT}(aa_H) = 0$ for the 14 May 1921 event as the largest aa_H value was during that storm. Hence, which storm is found to be the largest depends on which parameter is used to quantify it.

Part A of Figure 18 shows there is a strong anticorrelation between the peak of the mid-latitude geomagnetic index aa_H and the minimum of the (predominantly) ring current index Dcx ($r = -0.86$), as expected. There is also a good correlation between the minimum geomagnetic latitude of the aurora, Λ_M and the minimum Dcx ($r = 0.82$, part B) and a good, but slightly less strong, anticorrelation with the peak aa_H ($r = -0.77$, part C). These correlations are all significant at better than the 4σ level ($p < 1 \times 10^{-4}$) and in Parts A and C they are even significant at the 5σ level ($p < 6 \times 10^{-7}$). Hence, auroral event extent is certainly anticorrelated with deep minima in the ring current index Dcx and correlated with strong maxima in mid-latitude geomagnetic indices such as aa_H .

The bottom row of Figure 18 looks at the relationship to the area of the causal sunspot group, A_G . The correlations are weak with the geomagnetic responses and not as highly significant (significance levels are only 1σ in D and E but is at the 3σ level for F). Somewhat surprisingly, the causal group area A_G anticorrelates with all 3 terrestrial measures of enhanced activity (i.e. it correlates with the Dcx and the minimum Λ_M value, and anticorrelates with aa_H). Notice, however, the scatter is large and very low latitude aurora can result from a small group (as in the Secchi event) or a very large one (as in the Carrington event).

4 CONCLUSIONS

We have presented a survey based on 374.5 years of auroral observations. Our criteria for defining an extreme auroral event, in terms of how close to the magnetic equator it reaches, generates just 20 nights out of the total of 136786 nights in the interval: this is an occurrence of just 0.015% of nights. We use only data from the Northern Hemisphere in the interest of making the record as homogeneous as possible. All these events occur after the Dalton minimum. This may be because of poor observation records in the 17th and 18th centuries but the quieter solar conditions may also have contributed. If we take the interval of good observations to be from just before the start of the Dalton minimum to the present data (1790–2024.5), the percentage of nights giving events that meet our criterion rises to 0.023%.

We find that these events are always accompanied by a large geomagnetic storm, but many events of geomagnetic activity at or exceeding this level do not give an auroral event that meets our criteria. The events all occur around the peak of the solar cycle (a few are in the declining phase), but do not correlate well with sunspot number: indeed, both average auroral latitude and the number of extreme events is greater at moderately large sunspot number than at very high sunspot number.

Both nights of the event of 10–11 May 2025 qualify as extreme events, but they only rank as 3rd and 6th in our list of events, ranked by the lowest magnetic latitude reached. The greatest event, by far, is the Secchi event of 4 February 1872 which reached record lows in geomagnetic latitudes all around the globe.

The extreme auroral events do not occur at the minima of solar cycles but their occurrence is not otherwise controlled by the sunspot number. All these events occur when the open solar flux is very high but very high open flux does not guarantee an event will occur.

Looking at the areas of the sunspot groups from which the causal CME emerges, there are many very large-area groups that pass across the solar disc without giving a major auroral storm and although both large and small sunspot groups can give auroral superstorms overall there is a slight, but significant, anticorrelation between auroral and geomagnetic responses and the area of the sunspot group from which the responsible coronal mass ejection emerged.

ACKNOWLEDGEMENTS

The authors wish to thank many scientists and auroral enthusiasts who contributed dates and places of auroral sightings. Particular thanks go to Sam Silverman, who's extensive catalogues are available from NASA/NSSDC on request. We also thank a number of space weather internet sites that contributed recent sightings, in particular Spaceweather.com for the archive provided by their Auroral Image Gallery. We also thank the citizen science projects Aurorasaurus, AuroralReach and Skywarden which we searched for observations of the May 2024 event. We thank a number of datacentres: WDC-SILSO, Royal Observatory of Belgium, Brussels for the sunspot numbers used in this paper, the Heliophysical Observatory, Debrecen, Hungary for the Debrecen Photoheliographic Database, The University of Oulu for the Dcx index and the International Service for Geomagnetic Indices (ISGI) for the aa index data which we use to generate aa_H . We also thank the VIIRS Imagery and Visualization Team, CIRA, Colorado State University, USA for the whole oval auroral image composites and Will Dunn (WD Photography), Nick Bull (Stonehenge Dronescape), Maximilian-Vlad Teodorescu (Maximus Photography, Romania), Crystal Sibson (Crystal Sibson

Photography) and Giovanni Tessicini for the ground-based auroral images. ML and MJO are grateful to the UK Science and Technology Facilities Council (STFC), who part funded this work through grant number ST/V000497/1.

DATA AVAILABILITY

The dataset of auroral observations used in this paper is available on request from ML (m.lockwood@reading.ac.uk). It will be published as soon as we can, with a DOI, but we need to carry out some further work to expunge surviving duplicates and establish (and record) the true provenance (in terms of listing the catalogues it has previously been included in) for each of the 0.2 million records. Much of this work has been completed; however, the QD latitude for each observation needs to be added (at present it is computed for each auroral report in the software). Until this is completed, the author can provide the data and Matlab software to add the QD geomagnetic latitudes (which takes of order 10 minutes to run on the whole dataset on a standard laptop). The sunspot data used were generated by WDC-SILSO/SIDAC, Royal Observatory of Belgium, Brussels and are available from <https://www.sidc.be/SILSO/datafiles>. The sunspot group areas are retrieved from the Debrecen Photoheliographic Database <http://fenyi.solarobs.epss.hun-ren.hu/en/databases/DPD/>. The definitive D_{cx} index (at the time of writing, up to the end of 2016) is available from Oulu University at <http://dcx.oulu.fi/?link=queryDefinite> and provisional D_{cx} from <http://dcx.oulu.fi/?link=queryProvisional>. The homogeneous aa_H geomagnetic index is stored in the supplementary information files attached to the papers by Lockwood et al. (2018a) and Lockwood et al. (2018b).

REFERENCES

- Abbott W., Chapman S., 1959, *J. Atmos. Terr. Phys.*, 14, 111
 Alken P., et al., 2021, *Earth, Planets and Space*, 73, 49
 Allen J., Sauer H., Frank L., Reiff P., 1989, *Eos*, 70, 1479
 Angot A., 1896, *The Aurora Borealis*. Kegan Paul, Trench, Trubner & Co., London
 Antonova E. E., Stepanova M. V., Moya P. S., Pinto V. A., Vovchenko V. V., Ovchinnikov I. L., Sotnikov N. V., 2018, *Earth, Planets and Space*, 70, 127
 Bamba Y., Inoue S., Hayashi K., 2019, *Ap. J.*, 874, 73
 Baranyi T., Győri L., Ludmány A., 2016, *Sol. Phys.*, 291, 3081
 Berrilli F., Giovannelli L., 2022, *JSWSC*, 12, 3
 Boteler D. H., 2019, *Space Weather*, 17, 1427
 Boué A., 1856, *Acad. Wiss. Wien. Math. Phys.*, C1, 22
 Carapiperis L. N., 1956, *Geofis. Pure & Applic.*, 35, 139
 Case N. A., MacDonald E. A., 2015, *A & G*, 56, 3.13
 Cliver E., Dietrich W., 2013, *JSWSC*, 3, A31
 Cliver E., Schrijver C., Shibata K., Usoskin I., 2022, *LRSP*, 19
 Cyamungu M., et al., 2014, *IEEE Trans. Nuclear*, 61, 3667
 Denton M. H., Borovsky J. E., 2014, *JGR Space*, 119, 9246
 Emmert J., Richmond A., Drob D., 2010, *JGR Space*, 115, 2010JA015326
 Fritz H., 1873, *Fritz. H.: Verzeichnis beobachteter Polarlichter*. C. Gerold's Sohns, Vienna
 Frobesius J. N., 1739, *Luminis Atque Aurorae Borealis Spectaculorum Recensio Chronologica*. Christian Friedrich Weygandt, Helmstadt, Germany
 Frost A. M., Owens M. J., Macneil A., Lockwood M., 2022, *Sol. Phys.*, 297, 82:1
 González-Esparza J. A., Cuevas-Cardona M. C., 2018, *Space Weather*, 16, 593
 Grandin M., et al., 2024, *EGUsphere*, 2024, 1
 Green J. L., Boardsen S., 2006, *ASR*, 38, 130
 Győri L., Ludmány A., Baranyi T., 2017, *MNRAS*, 465, 1259
 Hapgood M., 2019, *Space Weather*, 17, 950
 Hayakawa H., et al., 2018a, *ApJ*, 862, 15
 Hayakawa H., Ebihara Y., Hand D. P., Hayakawa S., Kumar S., Mukherjee S., Veenadhari B., 2018b, *ApJ*, 869, 57
 Hayakawa H., et al., 2019, *MNRAS*, 484, 4083
 Hayakawa H., et al., 2021, *Ap. J.*, 909, 197
 Hayakawa H., Ebihara Y., Hata H., 2023a, *Geosci. Data J.*, 10, 142
 Hayakawa H., et al., 2023b, *Ap.J.*, 959, 23
 Hayakawa H., et al., 2024, *arXiv*, p. arXiv:2407.07665
 Ishkov V. N., 2016, *Vestn. Otd. nauk Zemle RAN*, 8, 1
 Jackson A., Jonkers A. R. T., Walker M. R., 2000, *Phil. Trans.*, 358, 957
 Jacobsen K. S., Andalsvik Y. L., 2016, *JSWSC*, 6, A9
 Kalb V., Kosar B., Collado-Vega Y., Davidson C., 2023, *Earth and Space Science*, 10, e2022EA002513
 Karinen A. K., 2005, *Ann. Geophys.*, 23, 475
 Kataoka R., Nakano S., 2021, *JSWSC*, 11, 46
 Kataoka R., Miyoshi Y., Shiokawa K., Nishitani N., Keika K., Amano T., Seki K., 2024, *Geophys. Res. Lett.*, 51, e2024GL108778
 Kistler L. M., 2020, *Geophys. Res. Lett.*, 47, e2020GL090235
 Kletzing C. A., Scudder J. D., Dors E. E., Curto C., 2003, *JGR Space*, 108, 2002JA009678
 Knipp D. J., Bernstein V., Wahl K., Hayakawa H., 2021, *JSWSC*, 11, 29
 Kosar B. C., MacDonald E., Case N., Y. Z., Mitchell E. J., Viereck R., 2018, *J. Atmos. Sol-Terr. Phys.*, 177, 274
 Kozyra J. U., Nagy A. F., Slater D. W., 1997, *Rev. Geophys.*, 35, 155
 Kubota Y., Nagatsuma T., Den M., Tanaka T., Fujita S., 2017, *JGR Space*, 122, 4398
 Křížský K., Pejml K., 1999, *Publ. Astron. Inst. Czechoslov. Acad. Sci.*, 75, 159–
 Lang A., 1849, *MNRAS*, 9, 148
 Laundal K. M., Richmond A. D., 2017, *Space Sci. Rev.*, 206, 27
 Liu Z., et al., 2024, *Geophys. Res. Lett.*, 51, e2023GL107209
 Livesey R. J., 1984, *J.B.A.A.*, 94(4), 158
 Livesey R. J., 2000, *J.B.A.A.*, 110 (6), 302
 Lockwood M., 2023, *JGR Space*, 128, e2023JA031671
 Lockwood M., Barnard L. A., 2015, *A&G*, 56, 4.25
 Lockwood M., Milan S., 2023, *Frontiers Astron. Space Sci.*, 10, 1139295
 Lockwood M., Owens M., 2024, *Sol. Phys.*, 299, 28
 Lockwood M., Owens M., Rouillard A. P., 2009a, *Journal of Geophysical Research: Space Physics*, 114, Article number A11103
 Lockwood M., Owens M., Rouillard A. P., 2009b, *Journal of Geophysical Research: Space Physics*, 114, Article number A11104
 Lockwood M., Chambodut A., Barnard L. A., Owens M. J., Clarke E., Mendel V., 2018a, *JSWSC*, 8, A53
 Lockwood M., Finch I. D., Chambodut A., Barnard L. A., Owens M. J., Clarke E., 2018b, *JSWSC*, 8, A58
 Lockwood M., Owens M. J., Barnard L. A., Haines C., Scott C. J., McWilliams K. A., Coxon J. C., 2020a, *JSWSC*, 10, 23
 Lockwood M., McWilliams K. A., Owens M. J., Barnard L. A., Watt C. E., Scott C. J., Macneil A. R., Coxon J. C., 2020b, *JSWSC*, 10, 30
 Lockwood M., Owens M. J., Barnard L. A., Watt C. E., Scott C. J., Coxon J. C., McWilliams K. A., 2020c, *JSWSC*, 10, 61
 Lockwood M., Owens M. J., Barnard L. A., Scott C. J., Frost A. M., Yu B., Chi Y., 2022a, *Front. Astron. Space Sci.*, 9, 960775
 Lockwood M., Owens M. J., Yardley S. L., Virtanen I., Yeates A., Muñoz-Jaramillo A., 2022b, *Front. Astron. Space Sci.*, 9, 976444
 Lockwood M., Owens M. J., Barnard L. A., 2023, *JGR Space*, 128
 Love J., Coisson P., 2016, *Eos*, 97, 18
 Love J. J., Hayakawa H., Cliver E. W., 2019a, *Space Weather*, 17, 1281
 Love J., Hayakawa H., Cliver E., 2019b, *Space Weather*, 17, 1281
 Love J., Rigler E., Hayakawa H., Mursula K., 2024, *JSWSC*, 14, 21
 Lovering J., 1868, *Mem. Am. Acad. Arts Sci.*, 10, 55
 Lyman H., 1921, *Mon. Weather Rev.*, 49, 406
 Mairan J. J., 1754, *de Ort, Traite Physique et Historique de l'Aurore Boreale*. Imprimerie Royale, Paris
 Mandal S., Krivova N., Solanki S., Sinha N., Banerjee D., 2020, *A&A*, 640, A78

- Mathieu E., Rodés-Guirao L., 2022, Our World in Data
- McNish A. G., 1941, *Terr. Mag. Atmos. Elec.*, 46, 461
- Meadows P., 2020, *MNRAS*, 497, 1110
- Meadows P., 2024, Journal BAA, 134, 215
- Mikhalev A. V., 2019, *Sol.-Terr. Phys.*, 5, 66
- Mikhalev A., 2024, *Sol.-Terr. Phys.*, pp 55–61
- Miyaoka H., Hirasawa T., Yumoto K., Tanaka Y., 1990, *Proc. Japan Acad., B*, pp 47–51
- Mursula K., Holappa L., Karinen A., 2011, *J. Atmos. Sol.-Terr. Phys.*, 73, 316
- Onsager T. G., Lockwood M., 1997, *Space Sci. Rev.*, 80, 77
- Oreshina A. V., Oreshina I. V., Somov B. V., 2012, *A&A*, 538, A138
- Owens M., Lockwood M., Barnard L., 2017a, *Sci. Rep.*, 7, 4152
- Owens M. J., Lockwood M., Riley P., Linker J., 2017b, *JGR Space*, 122, 10980-
- Owens M., Lockwood M., Barnard L., Scott C., Haines C., Macneil A., 2021, *Sol. Phys.*, 296, 82
- Pierrard V., Lopez Rosson G., 2016, *Ann. Geophys.*, 34, 75
- Pititsyna N. G., Demina I. M., 2021, *Geomagn. Aeron.*, 61, 312
- Rassoul H. K., Rohrbaugh R. P., Tinsley B. A., 1992, *JGR Space*, 97, 4041
- Rees M., 1969, *Space Sci. Rev.*, 10, 413
- Richmond A. D., 1995, *J.G.G.*, 47, 191
- Russell C. T., McPherron R. L., 1973, *J. Geophys. Res.*, 78, 92
- Sergeev V., Bondareva T., Gilles D., Donovan E., 2020, *J. Atmos. Sol.-Terr. Phys.*, 204, 105288
- Seydl A., 1954, *Geofys. S.*, 17, 159–
- Shao X., Cao C., Liu T.-C., Zhang B., Fung S. F., Sharma A., 2016, *IGARSS*, 2016, 3021
- Shepherd S. G., 2014, *JGR Space*, 119, 7501
- Shiokawa K., Yumoto K., Tanaka Y., Oguti T., Kiyama Y., 1994, *J. geomag. geoelect.*, 46, 231
- Shiokawa K., Miyoshi Y., Brandt P. C., Evans D. S., Frey H. U., Goldstein J., Yumoto K., 2013, *JGR Space*, 118, 256
- Silverman S., 1995, *J. Atmos. Terr. Phys.*, 57, 673
- Silverman S., 2006, *ASR*, 38, 136
- Silverman S., 2008, *J. Atmos. Sol.-Terr. Phys.*, 70, 1301
- Silverman S., Cliver E., 2001, *J. Atmos. Sol.-Terr. Phys.*, 63, 523
- Siscoe G., Crooker N., Clauer C., 2006, *Adv. Space Res.*, 38, 173
- Srivastava N., Mathew S., Louis R., Wiegmann T., 2009, *JGR Space*, 114, 2008JA013845
- Tinsley B. A., et al., 1984, *Geophys. Res. Lett.*, 11, 572
- Tinsley B. A., Rohrbaugh R., Rassoul H., Sahai Y., Teixeira N. R., Slater D., 1986, *JGR Space*, 91, 11257
- Valach F., Hejda P., Revallo M., Bochníček J., 2019, *JSWSC*, 9, A11
- Vichare G., Bhaskar A., Rawat R., Yadav V., Mishra W., Anghuk D., Singh A. K., 2024, Low-Latitude Auroras: Insights from 23 April 2023 Solar Storm, doi:10.48550/ARXIV.2405.08821
- Vázquez M., Vaquero J. M., 2010, *Sol. Phys.*, 267, 431
- Welling D. T., et al., 2015, *Space Sci. Rev.*, 192, 145
- Wolf R., 1857, *Vier. Nat. Ges. in Zürich*, 2, 253
- Wu C.-C., Liou K., Lepping R. P., Huttig L., Plunkett S., Howard R. A., Socker D., 2016, *Earth, Planets and Space*, 68, 151
- Yokoyama N., Kamide Y., Miyaoka H., 1998, *Ann. Geophys.*, 16, 566
- Zhang Q.-H., Lockwood M., Foster J. C., Zong Q., Dunlop M. W., Zhang S., Moen J. I., Zhang B., 2018, *Sci. Bul.*, 63, 31
- Zhao H., Zong Q.-G., 2012, *JGR Space*, 117, A11222
- van der Meeren C., Laundal K., Burrell A., Lamarche L., Starr G., Reimer A., Morschhauser A., 2023, *Zenodo*

This paper has been typeset from a \TeX / \LaTeX file prepared by the author.